

Supplementary Materials

Deep learning-based inverse design and forward prediction of bi-material 4D-printed facial shells

Mao-Chuan Chen¹, Yung-Ching Li¹, Yun-Yueh Yu¹, Yu-Ting Huang², Yung-Hsu Chen¹, Pei-Lin Hou¹, Yu-Cheng Tai¹, Jia-Yang Juang^{1,3,*}

¹Department of Mechanical Engineering, National Taiwan University, Taipei 106319, Taiwan.

²Department of Mechanical Engineering, Northwestern University, Evanston, IL 60208, USA.

³Program in Nanoengineering and Nanoscience, Graduate School of Advanced Technology, National Taiwan University, Taipei 106319, Taiwan.

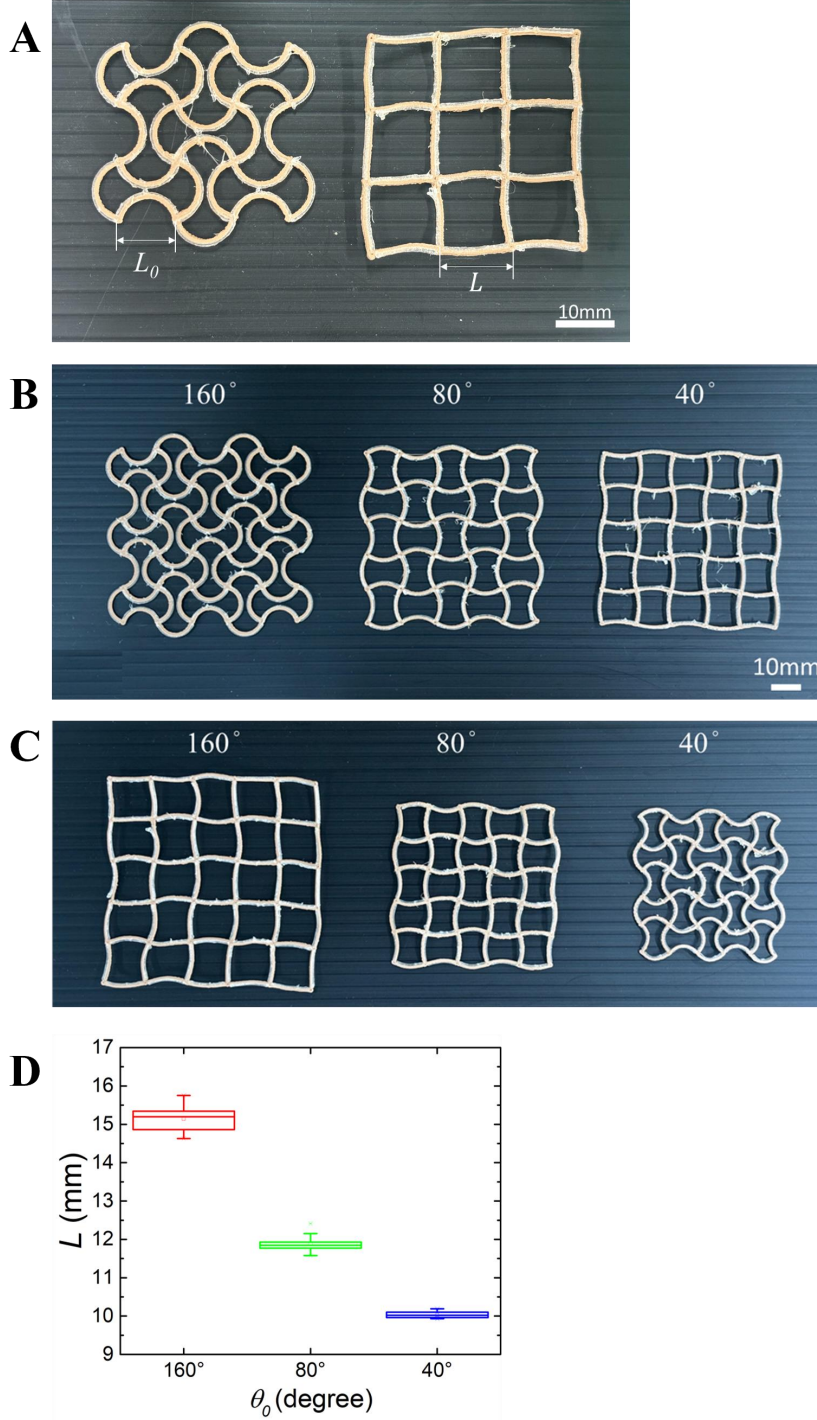
***Correspondence to:** Prof. Jia-Yang Juang, Department of Mechanical Engineering, National Taiwan University, Taipei 106319, Taiwan. E-mail: jiayang@ntu.edu.tw

Enhancing the Precision and Resolution of Depth Images

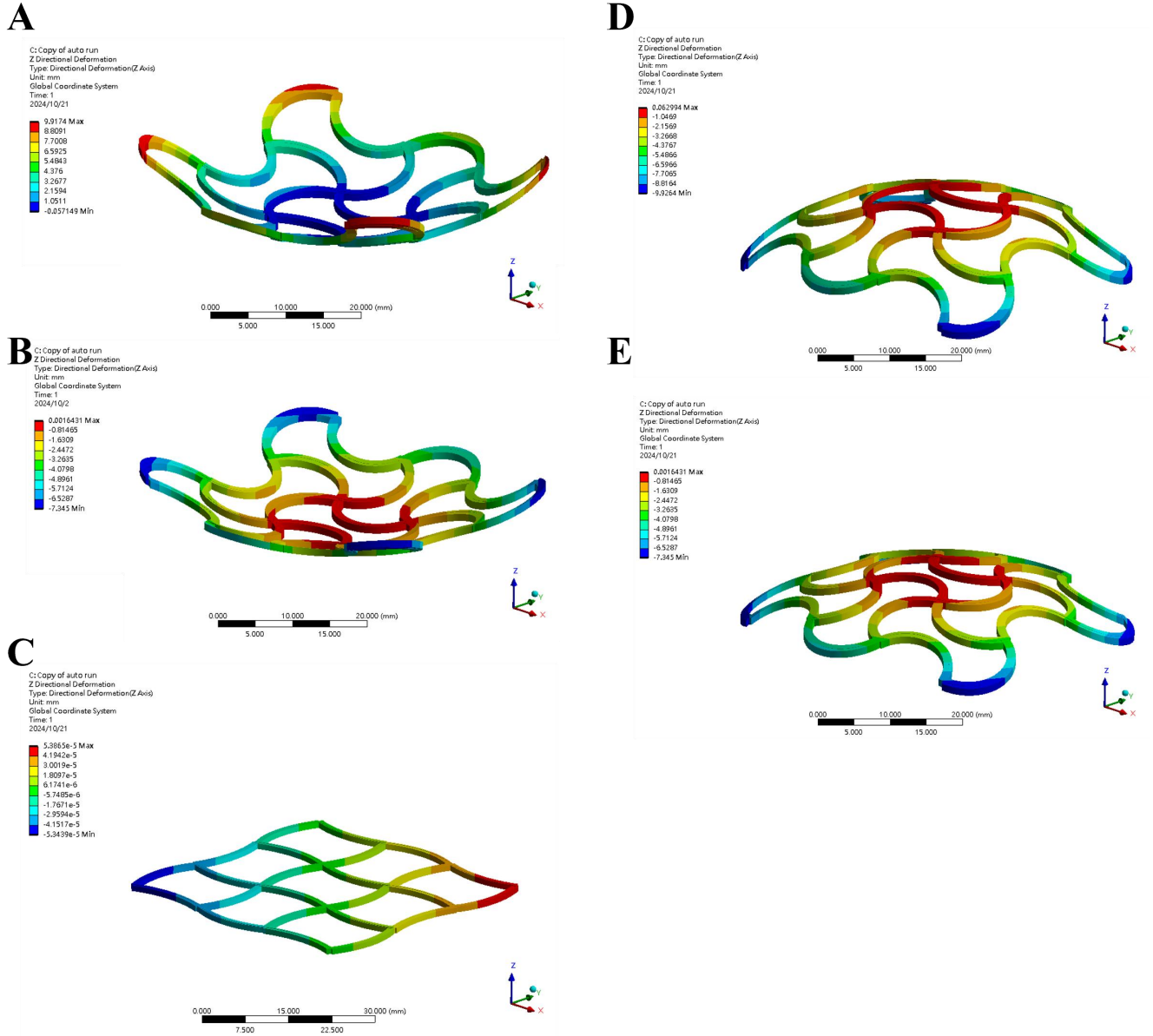
During depth image generation, since the simulation outputs values with up to 13 decimal places, rounding was applied to reduce unnecessary computation and facilitate the identification of the eye, nostril, and mouth openings. Specifically, values were rounded to the 10th decimal place to determine whether they were zero, while other values were rounded to the 4th decimal place. During node reduction, each grid unit retained only three points: two endpoints and a central point. The distance between the two endpoints was 0.0050 m, and the central point was located 0.0025 m from each endpoint. Based on conditional node statements, the node numbers corresponding to facial features (eyes, nostrils, and mouth) were identified. The `griddata` function from the SciPy library was used for linear interpolation based on Delaunay triangulation. The interpolation grid was set to 500×500 to enhance resolution and precision, and the `binary_r` colormap was applied to improve depth contrast. Because interpolation filled the openings of the eyes, nostrils, and mouth, these regions were overwritten with black (matching the background value) to preserve the correct mask openings.

3D Scanning

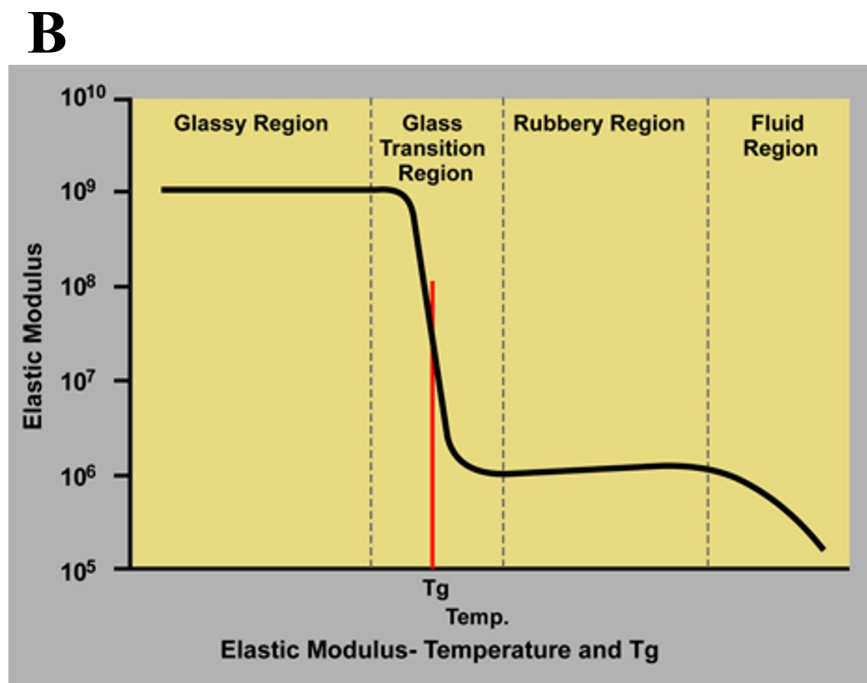
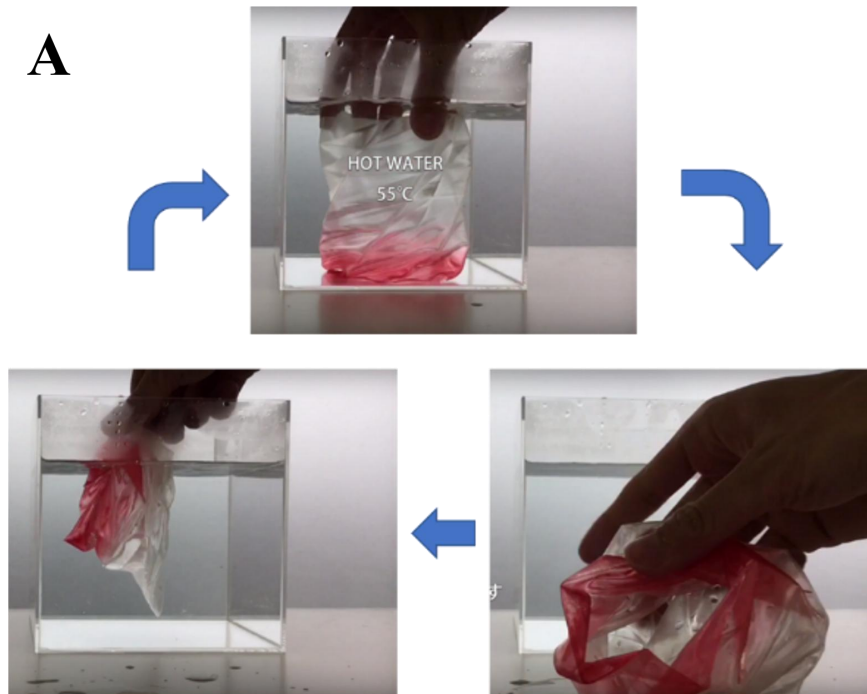
To keep the 3D gridshell suspended and stationary during scanning (Photos mode of the 3D Scanner app on the iPhone 14 Pro), fishing lines were attached to its top, left, and right design units. First, a horizontal scan was performed by keeping the camera parallel to the mask while circling around it to capture images. Next, an oblique upward scan was conducted, capturing images from a 45° angle above while circling the mask. Finally, an oblique downward scan was performed, capturing images from a 45° angle below. During each scan, a photo was taken approximately every 10° to fully capture the spatial information of the 3D gridshell. The 3D Scanner app reconstructed a 3D model from all photos and exported the point clouds as a .ply file. The three-dimensional coordinates of the data points were then extracted and saved as a .txt file to ensure consistency with the simulated node file.



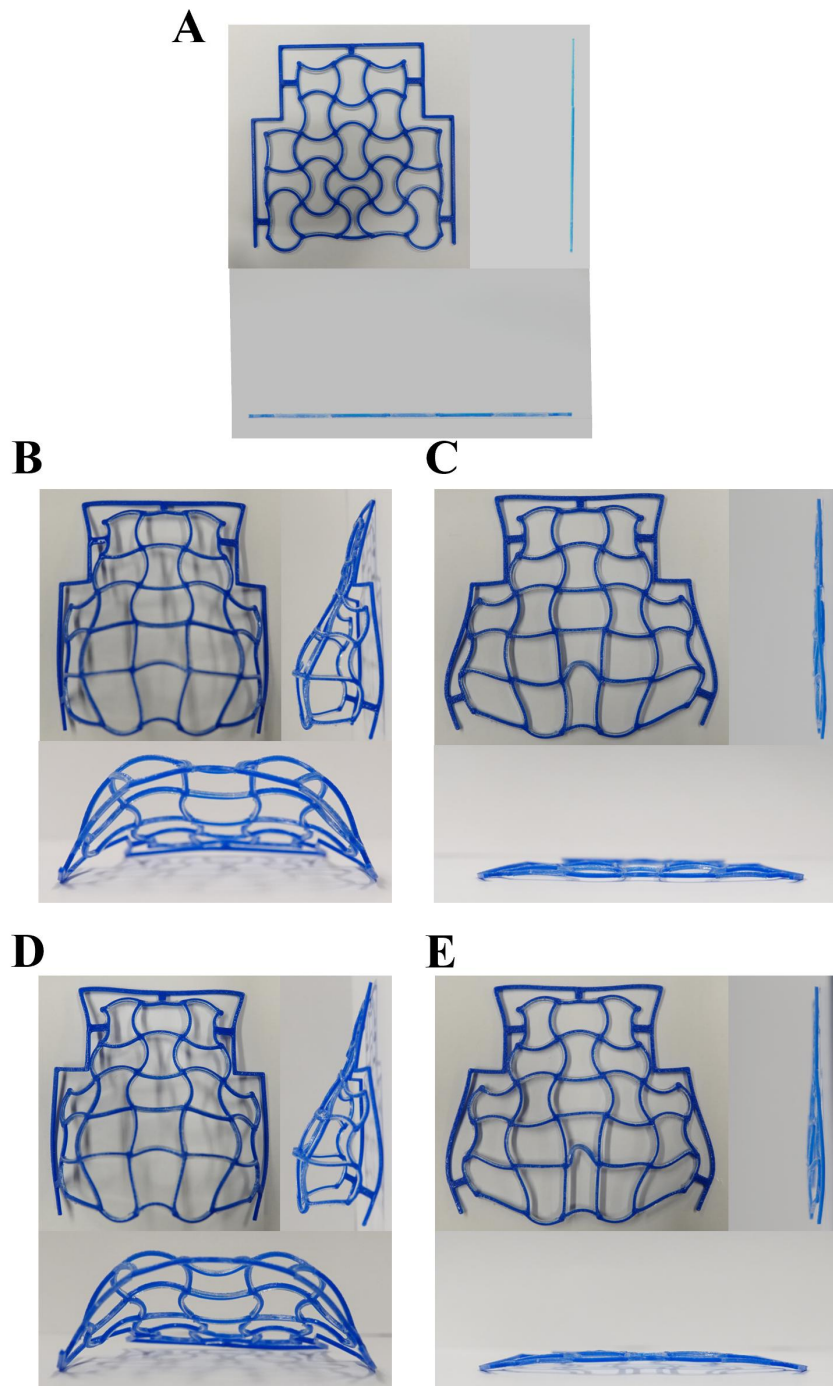
Supplementary Figure 1. Design concept and deformation behavior of the curved matrix inspired by heterogeneous lattices^[1]. (A) When the curved matrix is heated, the SMP undergoes greater contraction, pulling both ends of the rib inward toward the center. This action straightens the curved rib, resulting in elongation and increased node spacing. The initial node distance before deformation (L_0) was 12.5 mm, which increased to 15 mm (L) after deformation. Comparison of the homogeneous curve matrix at various angles: (B) before thermal activation, showing the initial geometry, and (C) after heating, illustrating the deformation behavior. (D) Relationship between curvature angle and elongation of the homogeneous curve matrix (with a standard deviation).



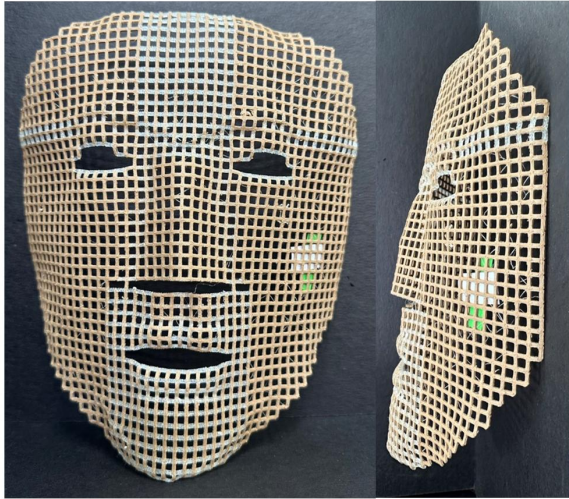
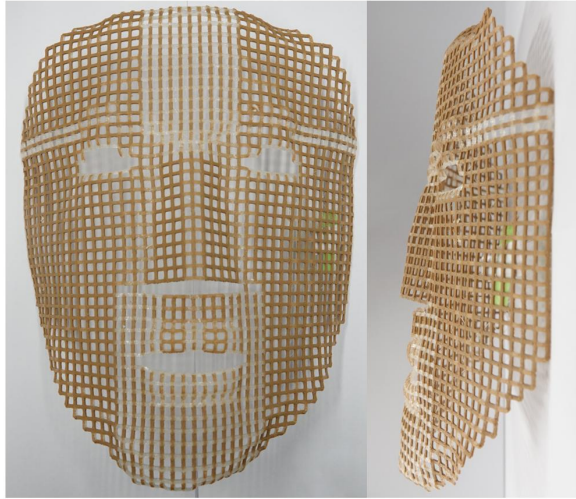
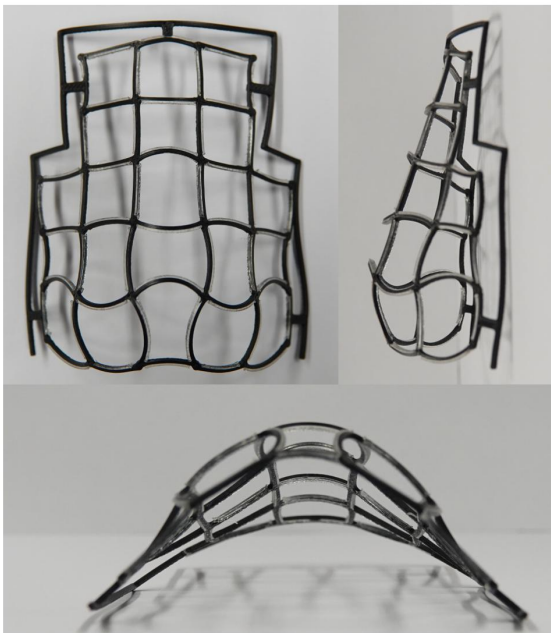
Supplementary Figure 2. Effect of material configuration on the deformation behavior of the structure at a sweep angle of 100° . (A) +4, (B) +2, (C) 0, (D)-2, (E) -4.



Supplementary Figure 3. Properties and thermal behavior of the shape memory polymer (SMP) used in this study. The SMP is a 3D printing filament developed by KYORAKU Co., Ltd. (Japan). When heated above 55 °C, corresponding to its glass transition temperature (T_g), its stiffness decreases by approximately three orders of magnitude. In this softened state, the material can be deformed into any temporary shape and subsequently returns to its original configuration upon reheating. (A) Thermal deformation and recovery process. (B) Variation of Young's modulus with temperature.



Supplementary Figure 4. Shape memory cycle of the curve matrix. (A) 3D-printed planar curved matrix; (B) deformation into a 3D thin shell after the first thermal activation; (C) reheated and flattened after the first cycle; (D) deformation into a 3D thin shell after the tenth thermal activation; (E) reheated and flattened after the tenth cycle.

A**B****C****D**

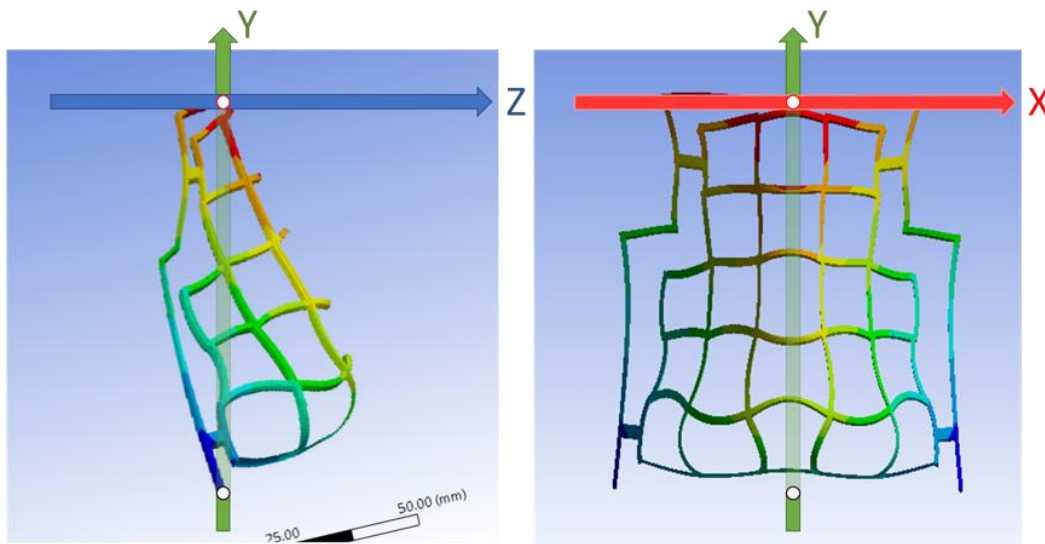
Supplementary Figure 5. Long-term stability of 3D thin shells following thermal activation. The line matrix images in (A) and (B) are separated by 15 months, and the curve matrix images in (C) and (D) are separated by 8 months, demonstrating sustained structural stability.



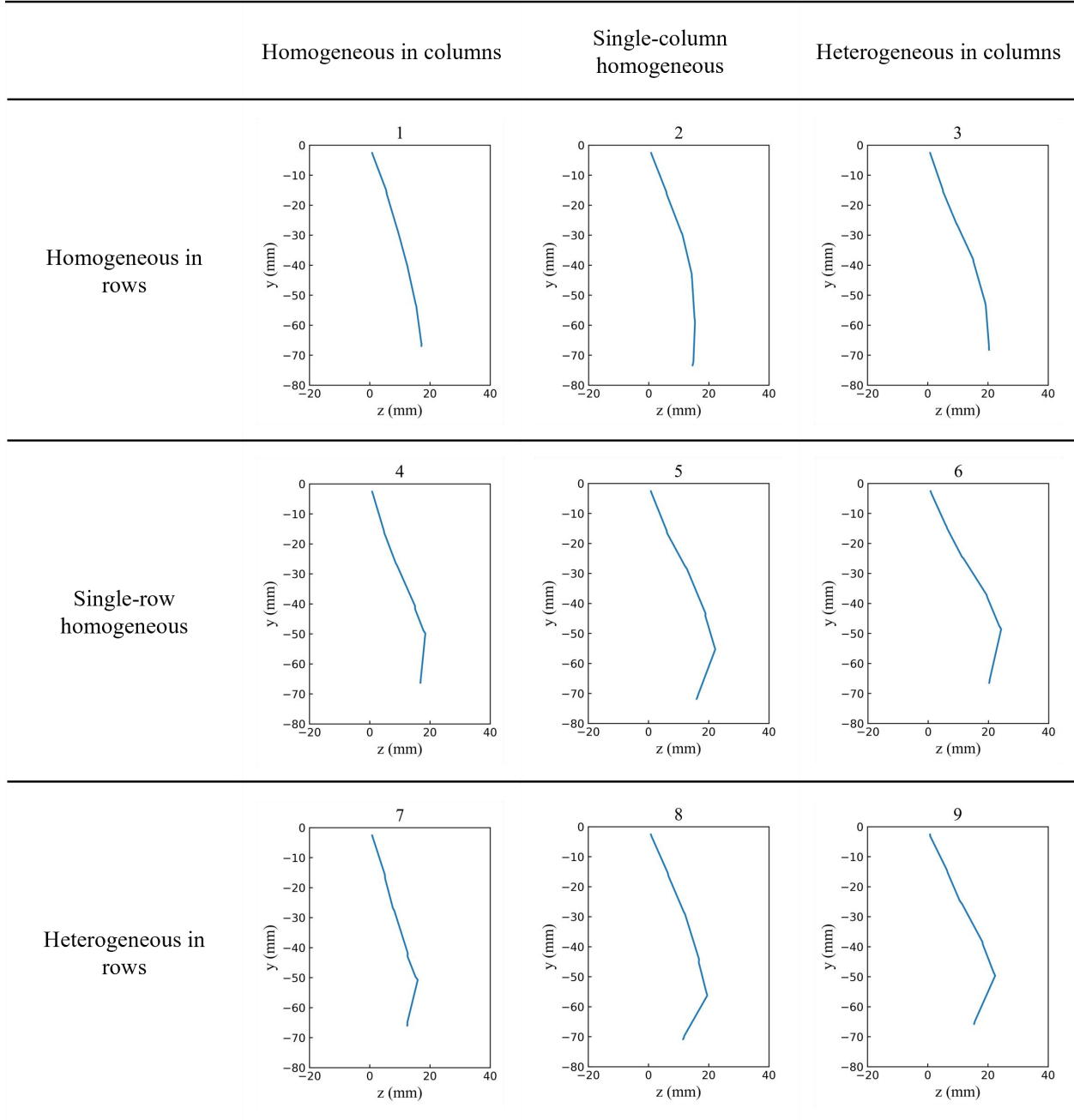
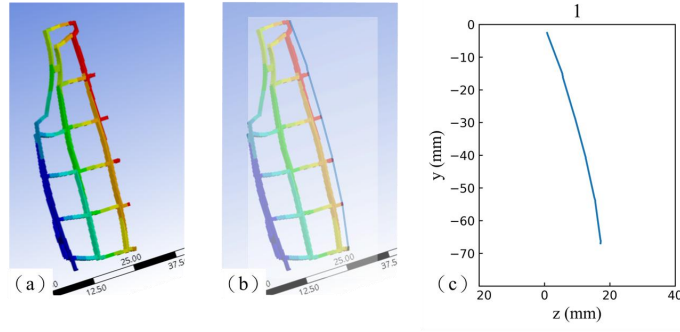
Supplementary Figure 6. Heterogeneity of the curve matrix. A curve matrix is considered heterogeneous when curvature angles vary within the same row or column. This variation arises from differing elongations of individual rib units. Rib units with greater elongation are constrained by neighboring units with lesser elongation, resulting in out-of-plane (three-dimensional) deformation.

	Homogeneous in columns	Single-column homogeneous	Heterogeneous in columns
Homogeneous in rows	1	2	3
Single-row homogeneous	4	5	6
Heterogeneous in rows	7	8	9

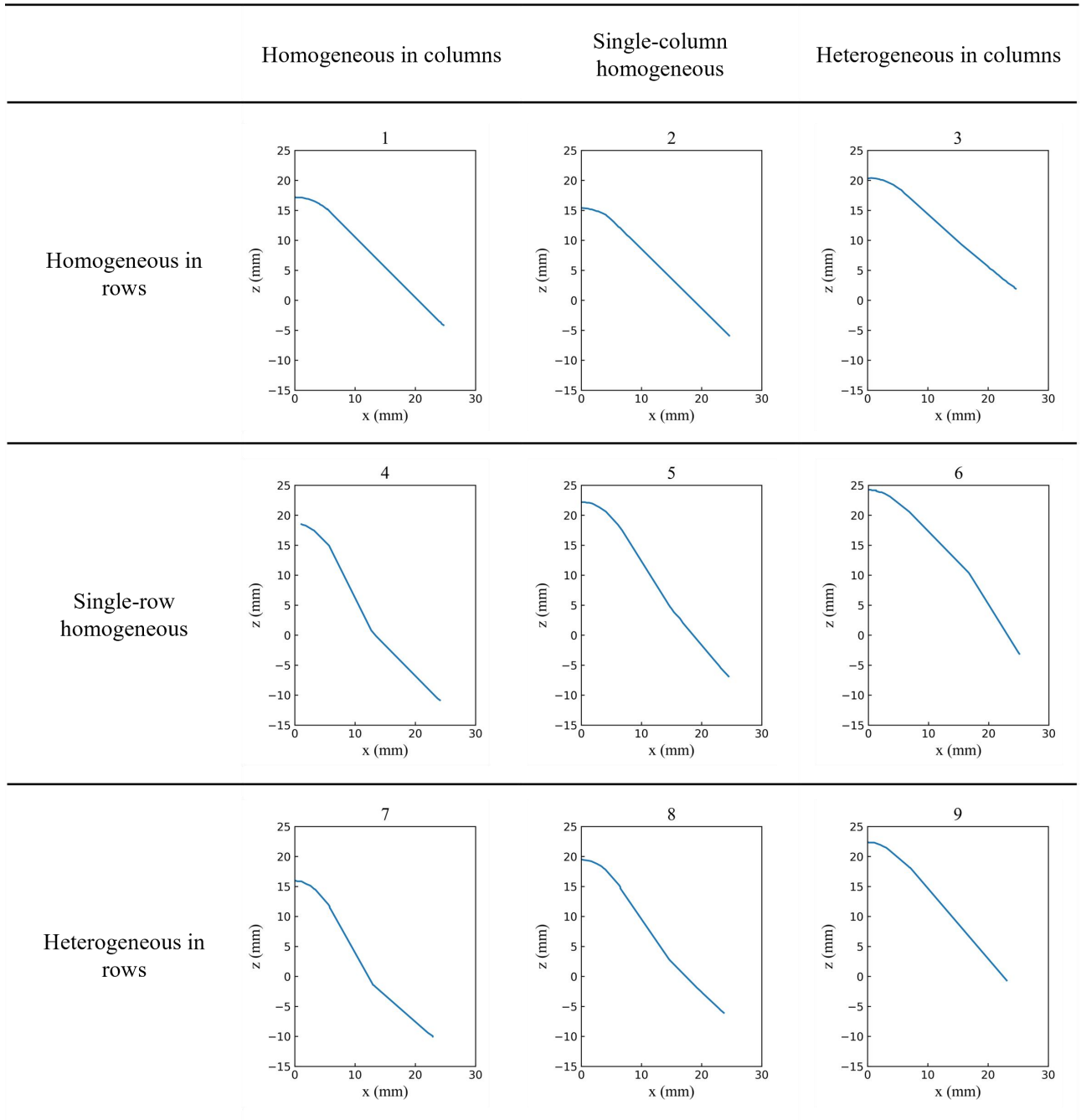
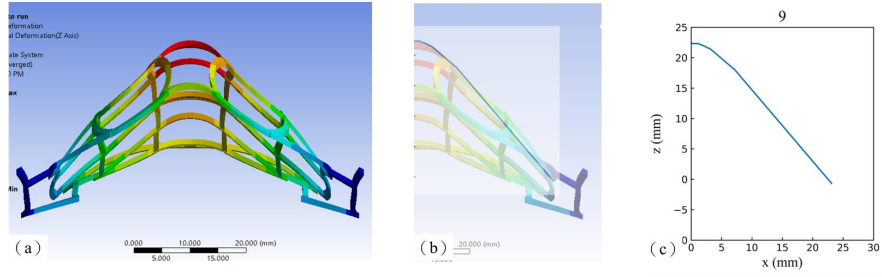
Supplementary Figure 7. Effect of different rib configurations on the deformation behavior of the nasal curve matrix. Homogeneous in columns indicates that all rib units within each column share the same curvature angle, while single-column homogeneous indicates that all rib units within each column share the same angle, with the angle gradually decreasing in columns farther from the center. Heterogeneous in columns indicates that the curvature angle is greatest at the nasal tip and gradually decreases along each vertical column. Homogeneous in rows indicates that all rib units within each row share the same curvature angle, whereas single-row homogeneous indicates that all rib units within each row share the same angle, with the angle gradually decreasing in rows farther from the center. Heterogeneous in rows indicates that the curvature angle is greatest at the nasal tip and gradually decreases along each horizontal row, following the same principle as the vertical configuration.



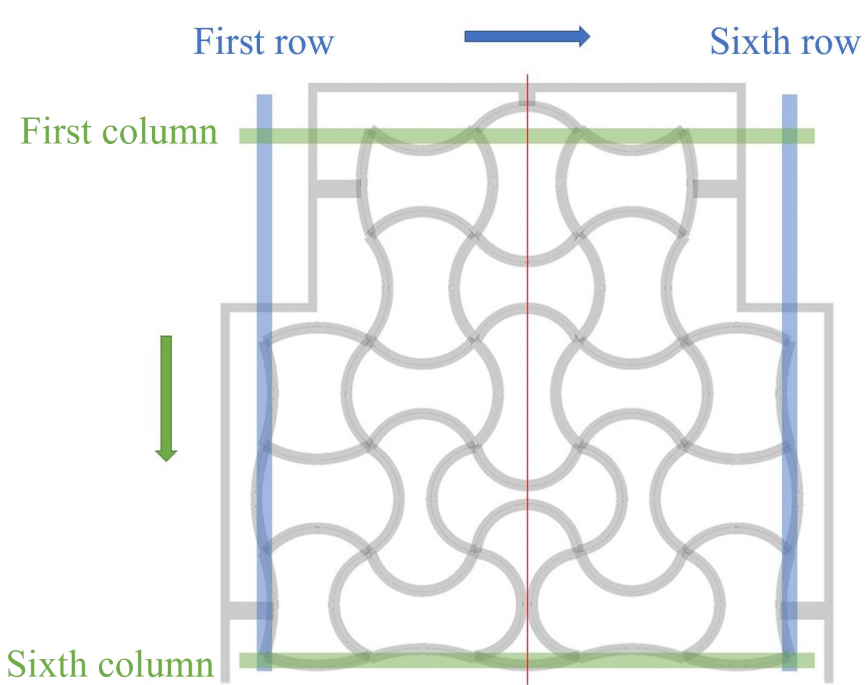
Supplementary Figure 8. Redefinition of coordinate axes for the nasal curve matrix to facilitate identification of key feature points and enable efficient data processing and comparison with anatomical measurements. The glabella point G is taken as the origin to establish the overall reference frame. One point at the end of each side of the nasal curved mesh framework (left and right) is selected, and the midpoint of the line segment connecting these points is calculated. The line passing through this midpoint and G defines the y-axis, with the upward direction along this line considered positive. The x-axis is aligned with the arrangement direction of the horizontal mesh nodes, and the z-axis direction is determined using the right-hand rule based on the plane formed by the x- and y-axes.



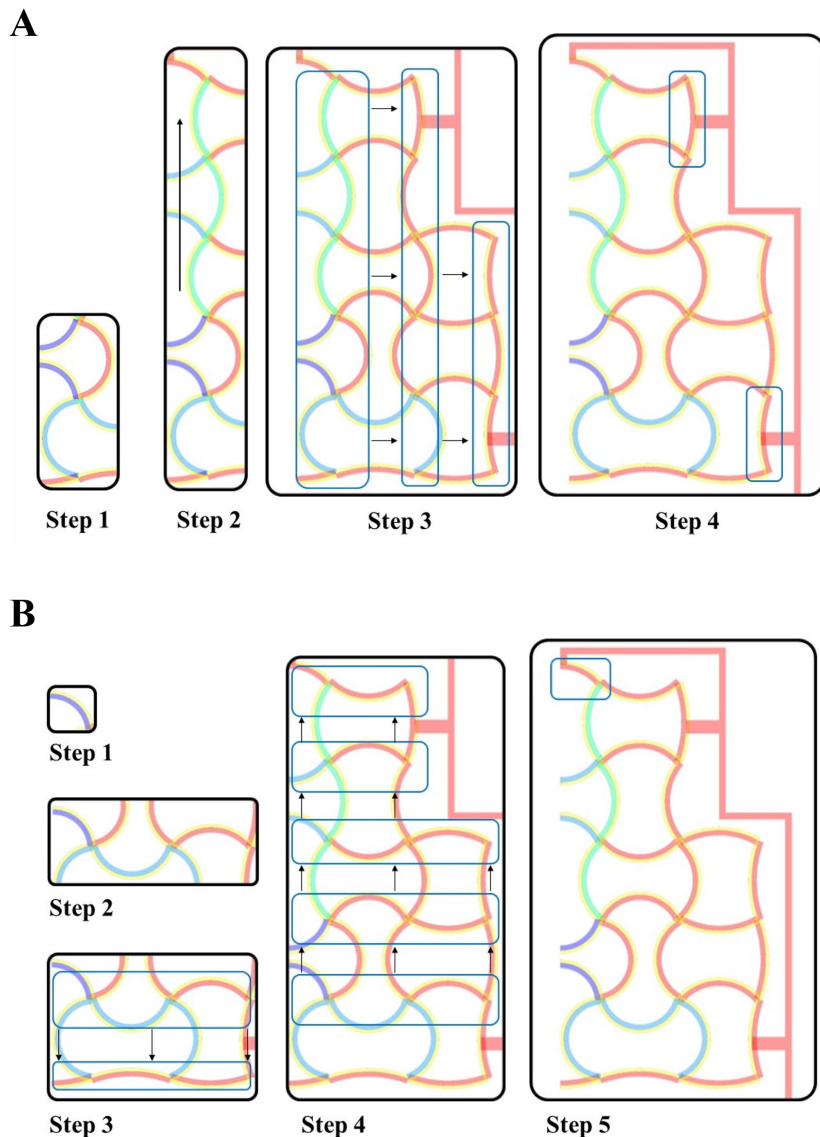
Supplementary Figure 9. Effect of different curve matrix configurations on the nasal bridge contour.



Supplementary Figure 10. Effect of different curve Matrix configurations on the nasal alar contour.

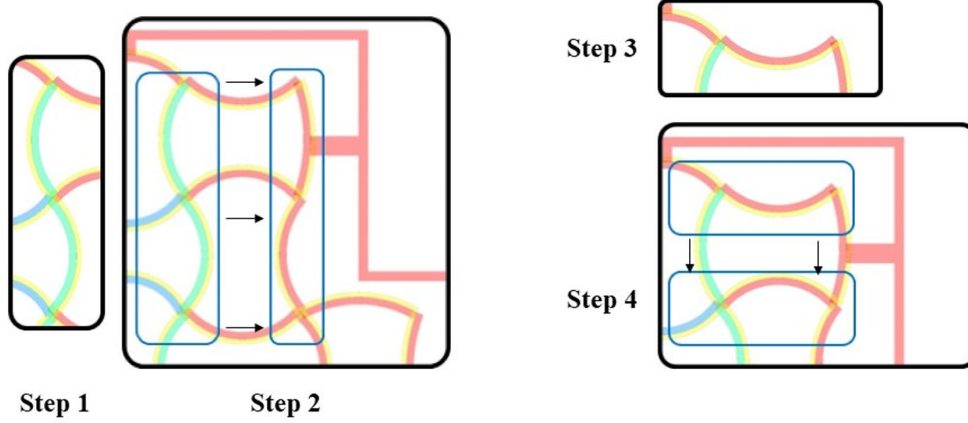


Supplementary Figure 11. Schematic diagram of row and column indexing for the nasal curved Matrix.

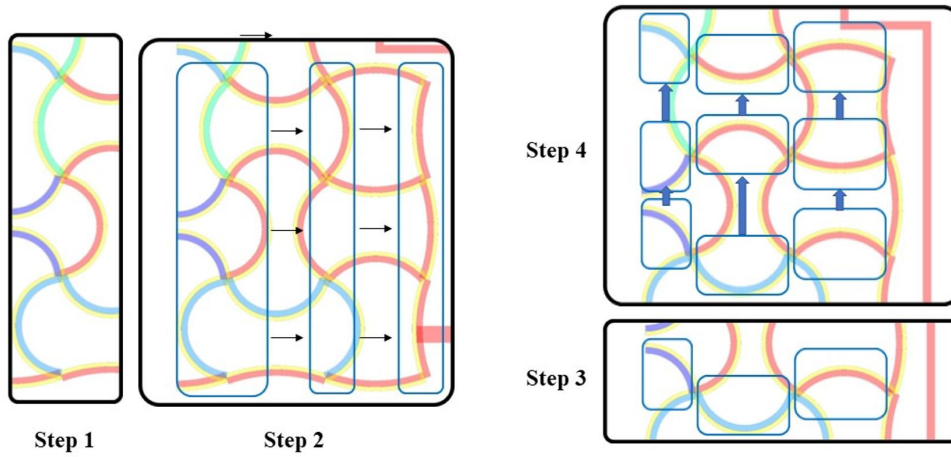


Supplementary Figure 12. Schematic diagram of the design process for random angle design in (A) Vertical columns. Step 1: The fourth or fifth rib in the fourth column is randomly selected as the nasal tip, and its angle is designated as the maximum angle of the curve matrix. Step 2: For the remaining ribs in the fourth column, their angles probabilistically decrease as their distance from the nasal tip increases. Step 3: The angle design of the fourth row is replicated in the fifth column, with a probabilistic reduction in angle. Subsequently, the configuration of the fifth row is replicated to the sixth column, again with a probabilistic reduction in angle. Step 4: Due to constraints imposed by the connecting frame, the angles of the two ribs located at the joint are fixed at 40 degrees. and (B) Horizontal rows. Step 1: The rib in the fifth row closest to the midline is designated as the nasal tip, and its angle is set as the maximum angle of the curve matrix. Step 2: For the remaining ribs in the fifth row, their angles probabilistically decrease as their distance from the nasal tip increases. Step 3: The angle design of the fifth row is replicated to the fourth row, with a probabilistic reduction in angle. This same strategy is applied to the remaining three rows above. Step 4: The angle design of the fifth row is also replicated to the sixth row, with a probabilistic increase or decrease in angle. Step 5: Due to structural constraints at the connecting frame, the angle of this rib at the joints is fixed at 100 degrees.

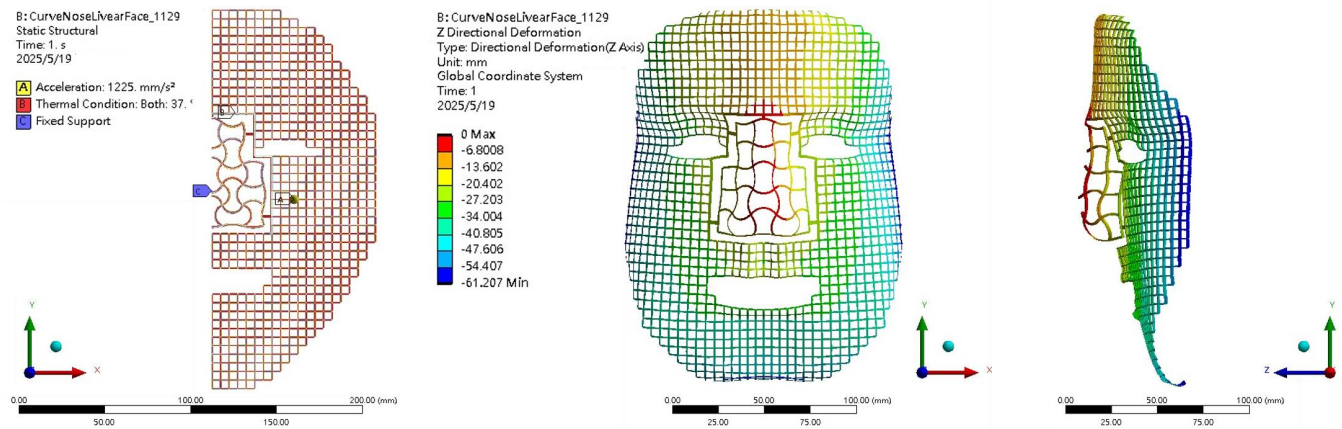
A



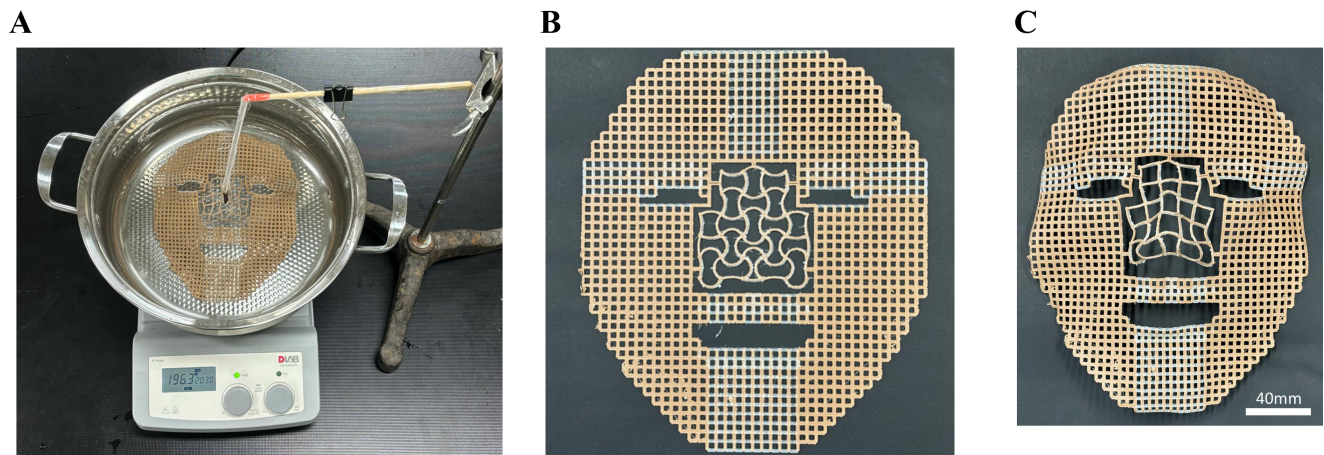
B



Supplementary Figure 13. Schematic diagram of the design process for random material design at (A) Nasal root. Step 1: The material design of the ribs in the fourth column is randomly assigned from the set $[-2, 0, +2, +4]$. Step 2: The material design of selected ribs in the fourth column is replicated to the fifth column, with each replicated value randomly multiplied by either 0 or 1. Step 3: The material design values of the ribs in the first column are randomly assigned from the set $[-4, -2, 0]$. Step 4: The material design of selected ribs in the first column is replicated to the second column, with each replicated value randomly multiplied by either 0 or 1. (B) Alar regions. Step 1: Based on the angle design of the sixth row, the material design of the ribs in the fourth column is randomly assigned from the set $[-4, -2, 0, +2, +4]$. Step 2: The material design of the fourth column is replicated to the fifth column, with each replicated value randomly multiplied by either 0 or 1. The same process is applied to the sixth column. Step 3: The material design of the ribs in the fifth row is randomly assigned from the set $[-4, -2, 0, +2, +4]$. Step 4: The material design of the fifth row is replicated to the fourth column, with each value randomly multiplied by either 0 or 1. The same procedure is applied to the third row.



Supplementary Figure 14. Simulation of deformation observed in the hot water immersion experiment under identical boundary conditions, with systematic adjustment of Young's modulus and thermal expansion coefficient.

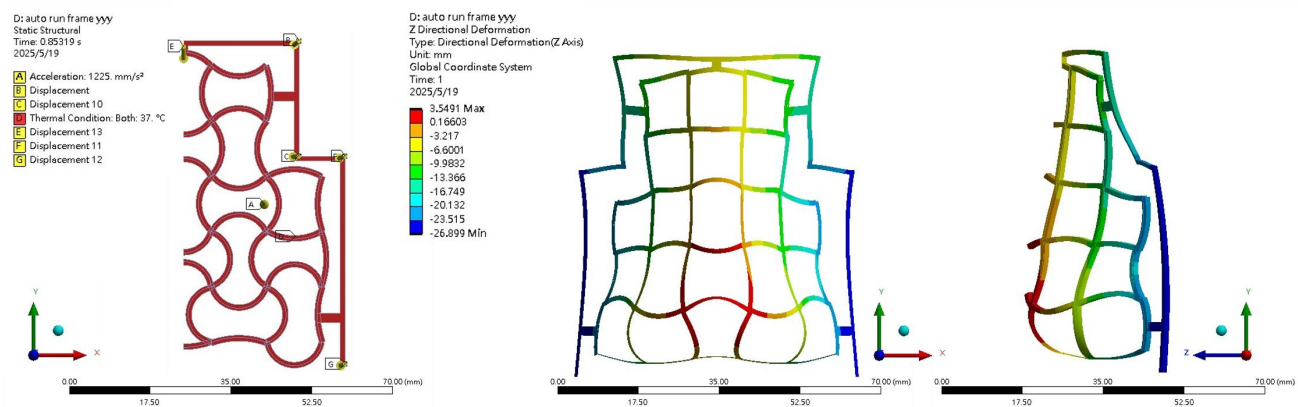


Supplementary Figure 15. (A) Hot water experimental setup. (B and C) Planar design transforming into the shell structure upon thermal stimulation.

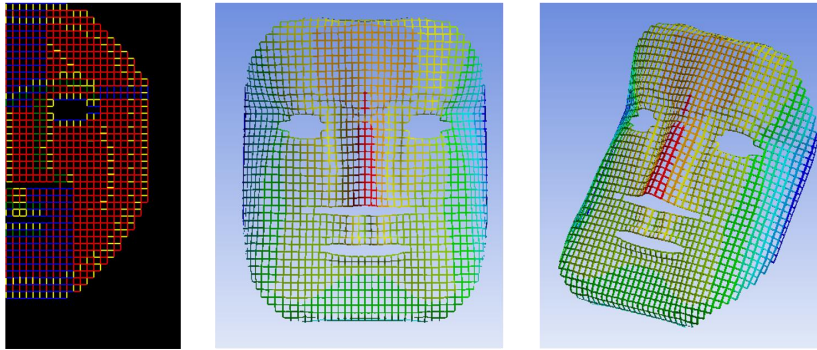
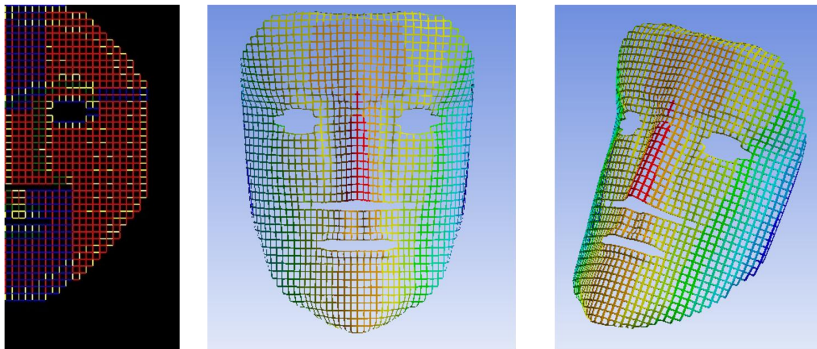
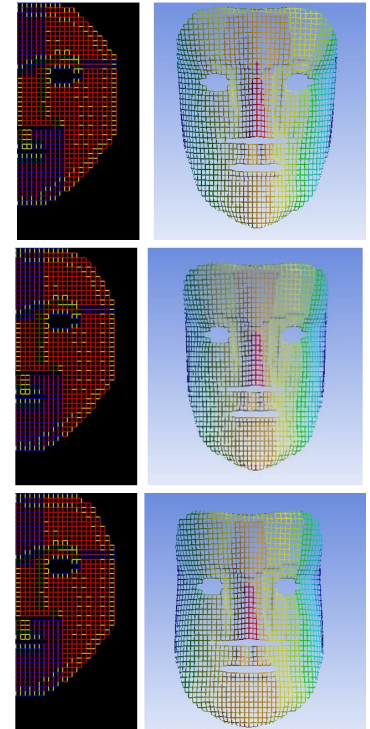
Supplementary Table 1. Comparison of simulation material parameters between line matrix and curve matrix

	Line matrix		Curve matrix	
	SMP55	PLA	SMP55	PLA
Youns's modulus, E_y	3.3	26	3.3	1.7
Poisson's ratio, γ	0.44	0.44	0.44	0.44
Coefficient of thermal expansion, α ($^{\circ}\text{C}^{-1}$)	-0.01	-0.00001	-0.02	-0.00001

When the simulation setups from the line matrix were applied to the curve matrix, the resulting deformation was insufficient and failed to match the experimental data. Through multiple rounds of parameter tuning and analysis, it was found that an insufficient Young's modulus and an excessively large thermal expansion coefficient led to non-convergence in the simulation.

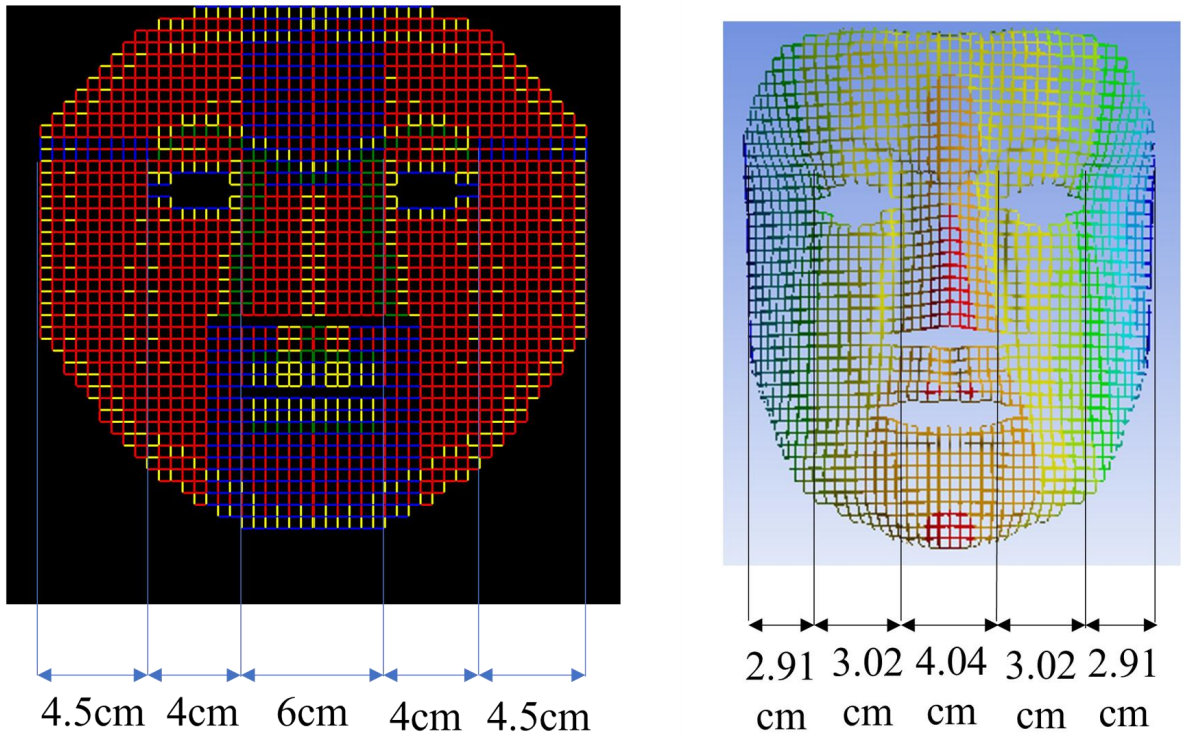


Supplementary Figure 16. Simplified model used to evaluate the feasibility of inverse design for the curve matrix and to accelerate simulation database generation.

A**B****C**

Supplementary Figure 17. Refinement of global curvature and chin configuration, with design (A) before and (B) after the adjustment. (C) Deformation results under different upcurve parameters, in sequence: 3, 4, and 5.

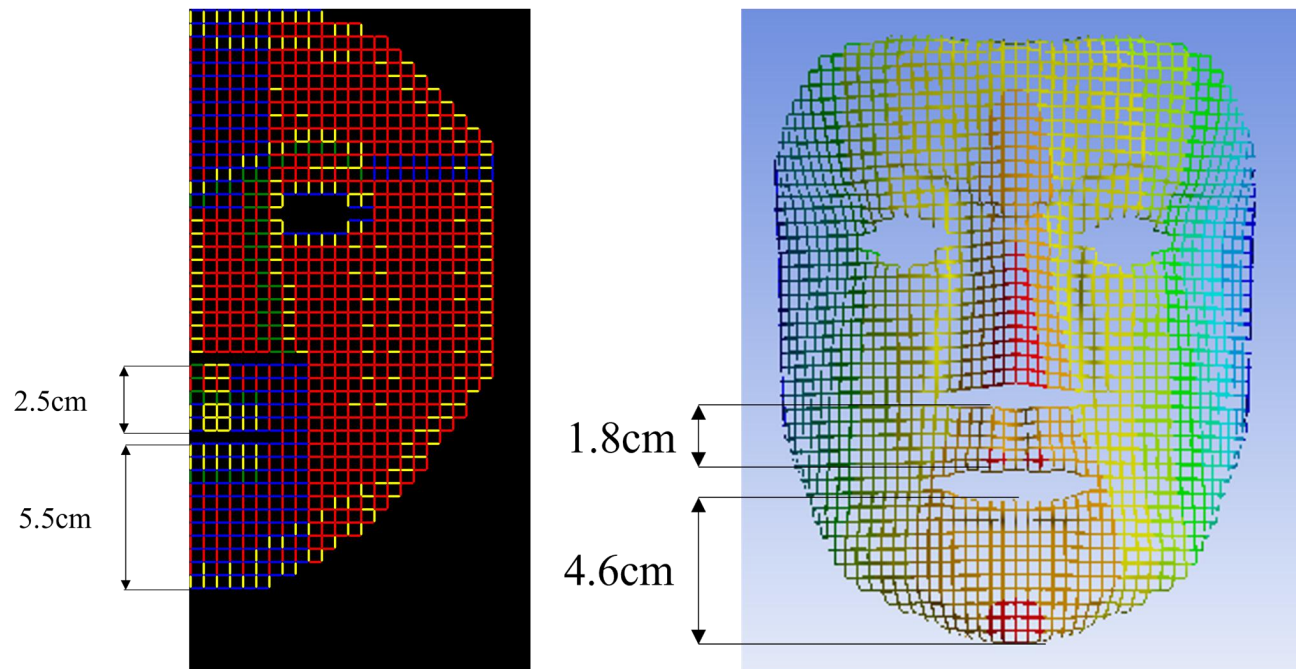
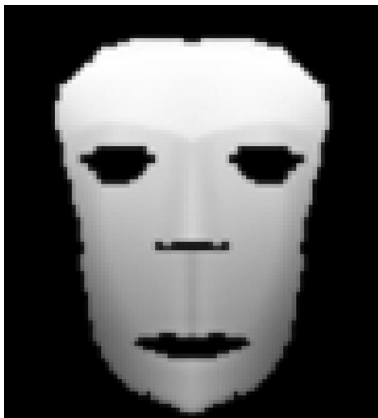
A



B



Supplementary Figure 18. (A) Schematic diagram of eye shape and interocular distance ratio. (B) Examples of previous mask designs: in the left image, the interocular distance is too wide and the eyes are positioned too close to the facial contour; in the right image, the interocular distance is too narrow. The interocular distance-to-face width ratios are 0.347 and 0.235, respectively, while the eye-to-contour-to-face width ratios are 0.091 and 0.146.

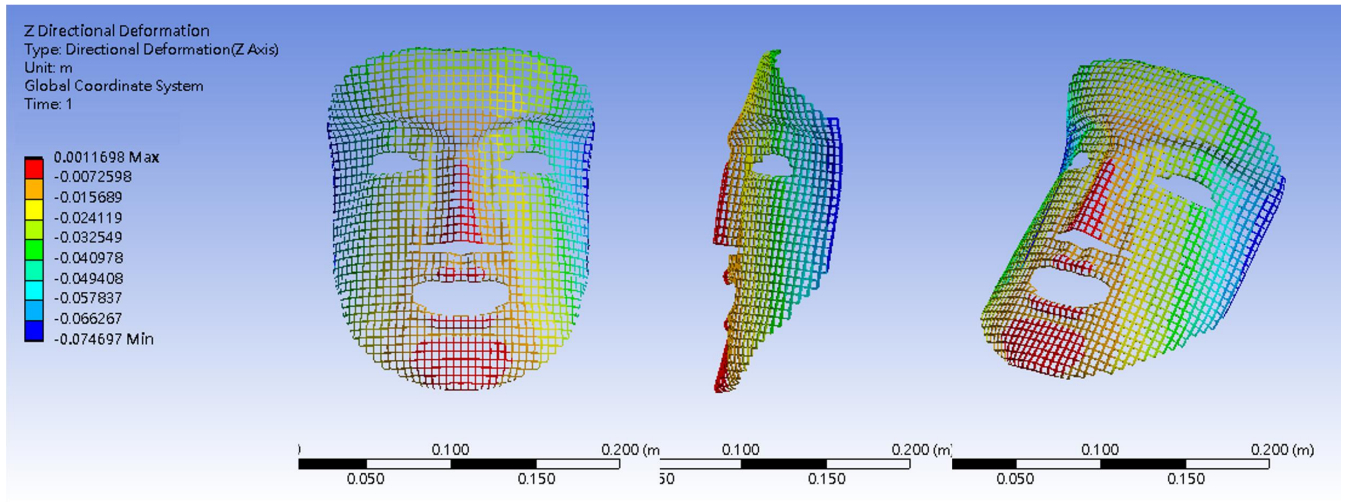
A**B**

Supplementary Figure 19. (A) Schematic diagram of the philtrum-to-chin length ratio. (B) An example from a previous mask design study showing an excessively long philtrum, with a philtrum-to-chin length ratio of 1.48.

Supplementary Table 2. Parameters of parametric polynomial functions in grid design

Feature	Parameter	Range
Brow Ridge	brow_dis	[3, 4]
	brow_height	[1, 2]
Eye	eye_x	[4, 6]
	eye_width	[5, 8]
	eye_height1	[1, 3]
	eye_height2	[1, 2]
	eye_rd	[4, 6]
	eye_tip	[-3, 3]
Nose	nose_b1	[3, 6]
	nose_b3	[8, 11]
	nose_p2	[0, 1]
	nose_p[0]	[-1, 2]
	nose_p[1]	[-1, 2]
	nose_w1	[2, eye_x-2]
	nose_w2	[3, 6] /4*nose_w1
Mouth	mouth_height	[1, 3]
	mouth_width	[5, 9]
	mouth_downb	[12, 20]
	mouth_upa	[8, 12]
	mouth_downa	[8, mouth_upa]
	mouth_upb	[9, 10]
	lip_t	[1, 2]
	philtrum	[1, 2]
Contour	upcurve	3
	downcurve	2
Space Adjustment	aspect ratio	[0.85, 1.15]
	length of upper face (from the hairline to the brow ridge)	[round(face_length/3) - 1.5, round(face_length/3) + 1.5]
	length of philtrum	[round(((face_length - nose_b3 - mouth_height - eye_y)/3 - 1.5), round(((face_length - nose_b3 - mouth_height - eye_y)/3 + 1.5))]

A



B



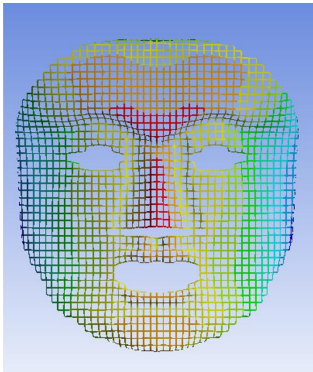
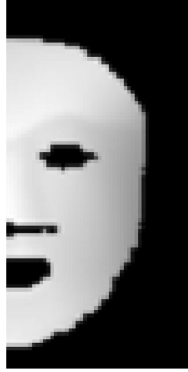
C



Supplementary Figure 20. Coordinate transformation aligning the z-axis with the mask's depth. (A) The same grid design. (B) The depth image before coordinate transformation. (C) Establishment of a new z-axis using the normal vector extending from the chin to the forehead. Two key points are identified on one half of the face: one at the bottom of the chin and one at the top of the forehead. This normal vector defines the new z-axis to avoid errors in depth information.

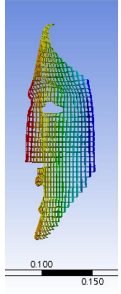
A**B**

Supplementary Figure 21. Boundary range of each shell in the XY coordinates was fixed for (A) mask and (B) nose, with depth values defined based on the height range of the thin shell. Units in meters.

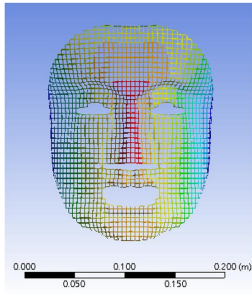
A**B****C****D**

Supplementary Figure 22. Comparison of depth images under previous and current specifications. (A) Same 3D grid shell. (B) Previous study specifications, with pixel resolution increased from 101×50 to 400×200 . (C) Resolution enhancement to 400×200 pixels using the proposed method. (D) Upward translation at the same 400×200 pixels. Based on the operational characteristics of the FCN, the format and resolution of the depth images were optimized to improve the model's accuracy and generalization capability.

Side View



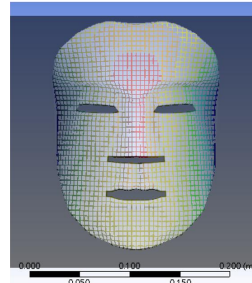
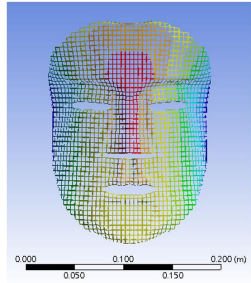
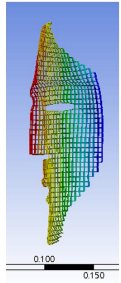
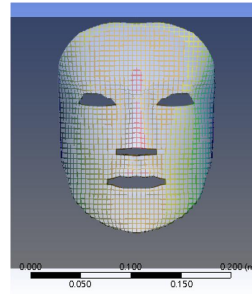
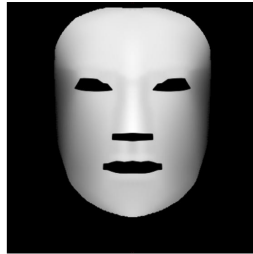
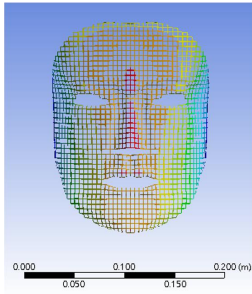
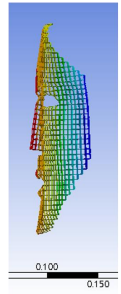
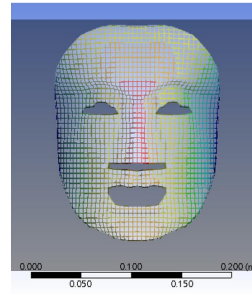
Frontal View



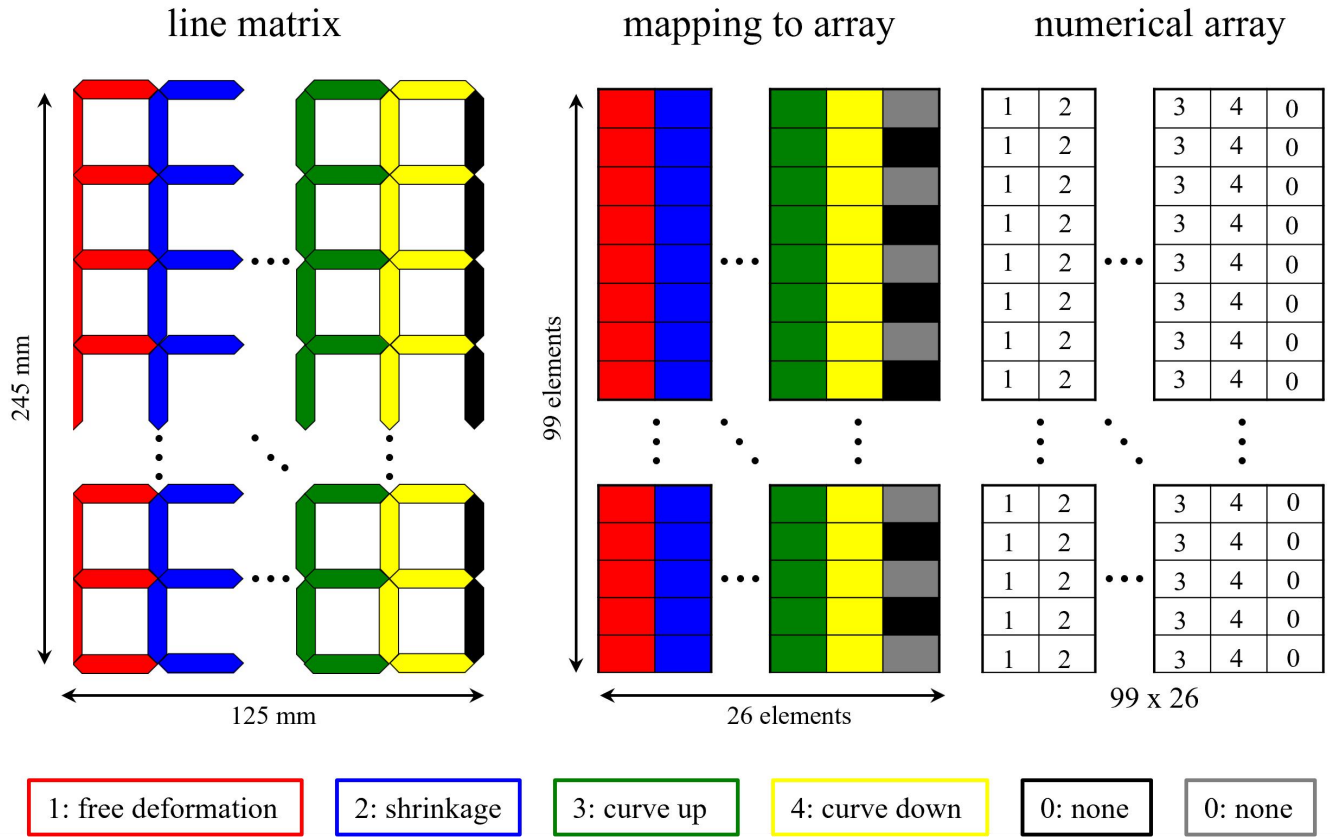
Depth Image



Overlay

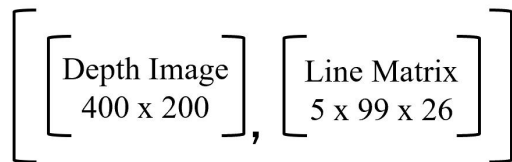


Supplementary Figure 23. Side-view result with the depth direction aligned parallel to the z-axis. Frontal simulation results are overlaid with depth images to verify the accuracy of the eye, nostril, and mouth contours, ensuring consistency between the grid shell and its corresponding depth image.

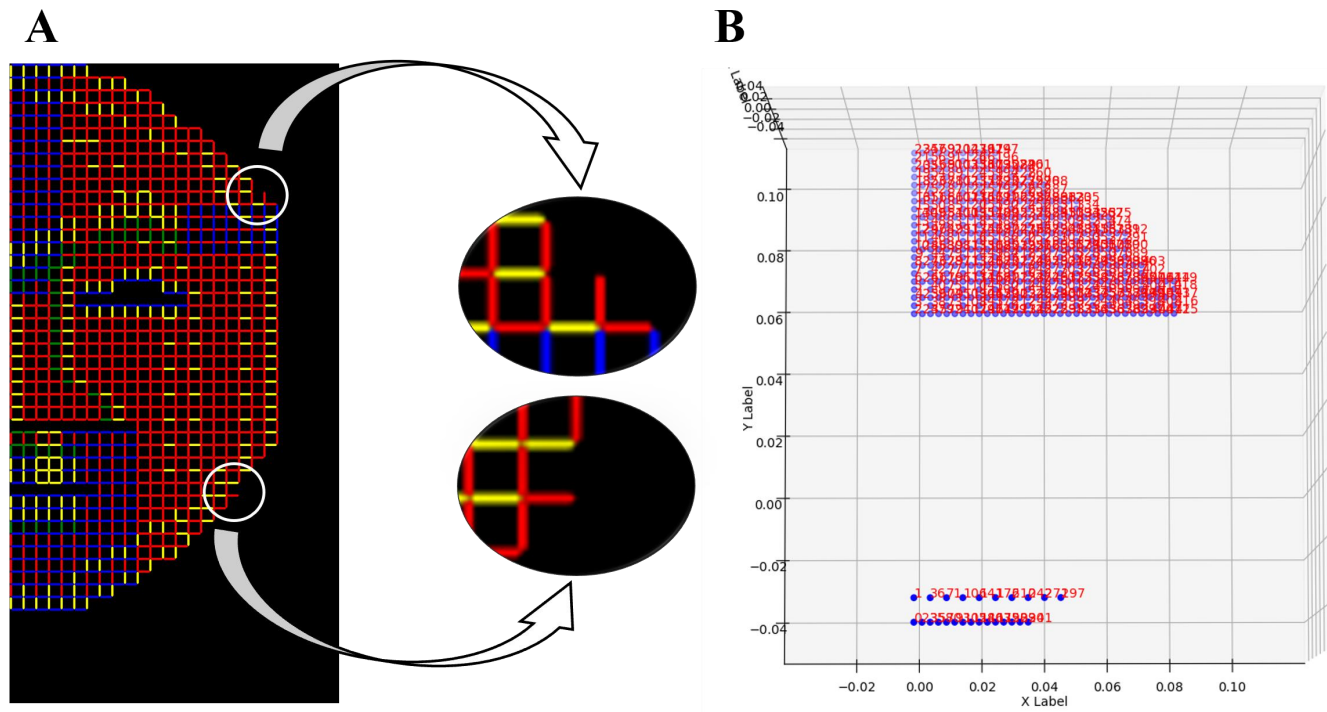


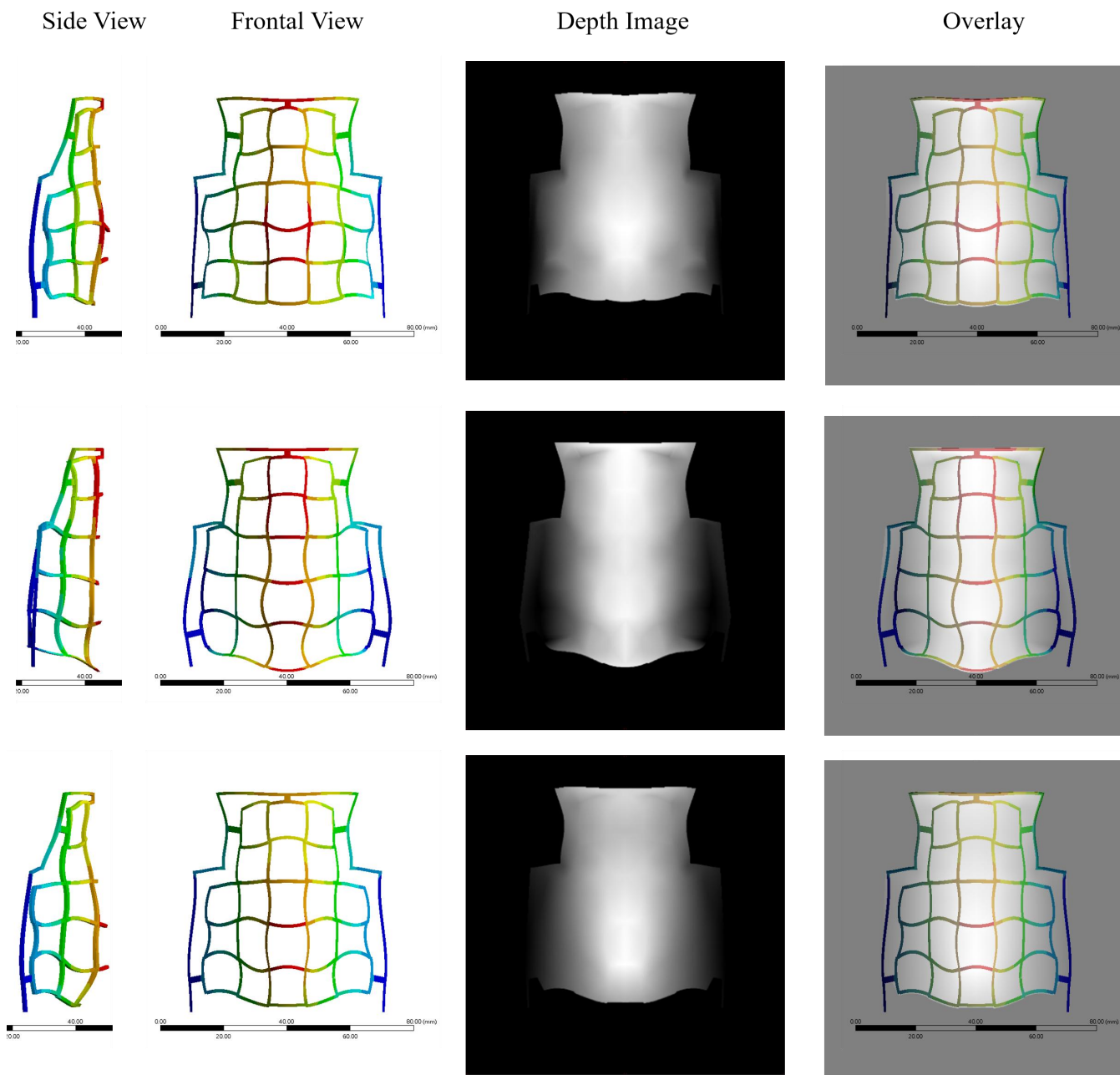
Supplementary Figure 24. Representation of grid design space both in structure and array.

Data format of deep learning in the line matrix (.npz)

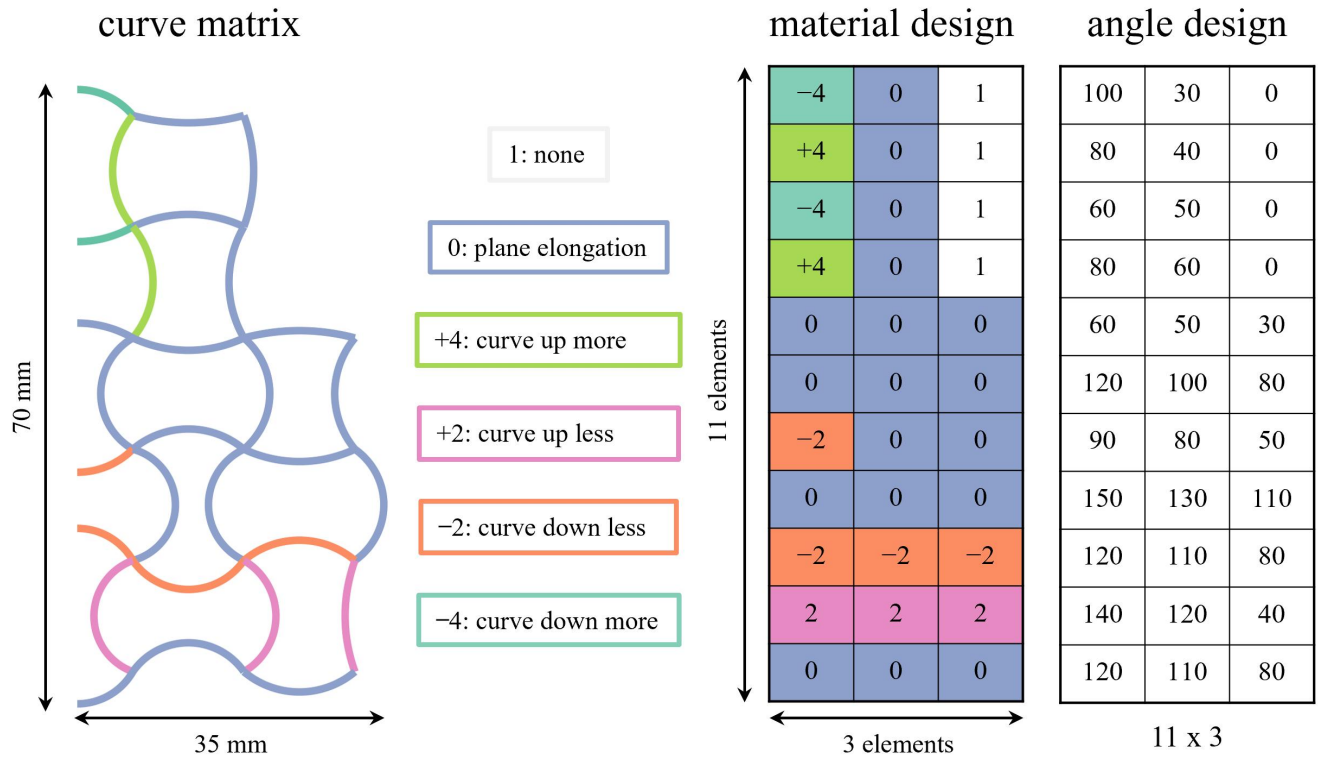


Supplementary Figure 25. Structure of .npz file in the line matrix.





Supplementary Figure 27. Frontal simulation results overlaid with depth images to verify the accuracy of the nose contour and connecting frame, ensuring consistency between the rib shell and its corresponding depth image.







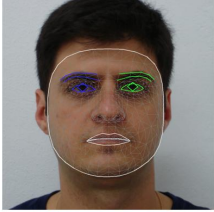







Supplementary Figure 28. Representation of rib design space both in structure and array.

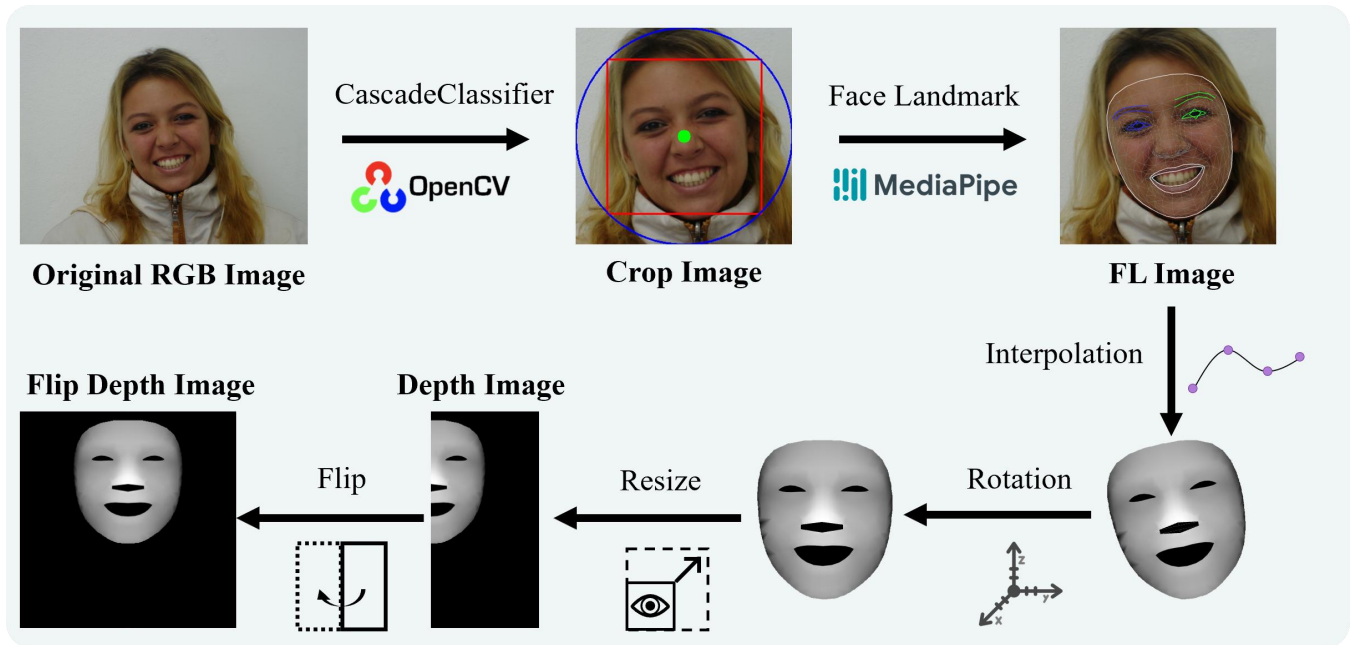
Data format of deep learning in the curve matrix (.npy)

$$\left[\begin{bmatrix} \text{Depth Image} \\ 400 \times 200 \end{bmatrix}, \begin{bmatrix} \text{Material Design} \\ 6 \times 11 \times 3 \end{bmatrix}, \begin{bmatrix} \text{Angle Design} \\ 1 \times 11 \times 3 \end{bmatrix} \right]$$

Supplementary Figure 29. Structure of .npy file in the curve matrix.

Dataset	Original RGB Image	Crop Image	Face landmark Image	Flip Depth Image
Chicago Face Database				
FEI Face Database				
Face Research Lab - London Set				

Supplementary Figure 30. Three public face databases used to generate depth images automatically. First, the Chicago Face Database (CFD) was developed by the University of Chicago and contains high-resolution frontal facial images of individuals aged 17 to 65 from diverse racial backgrounds, including Asian, Black, Latino, White, and Indian. All individuals in the database display a neutral facial expression, and the images have a 2444×1718 pixels resolution. Second, the FEI face database is a Brazilian face database that contains a set of face images taken between June 2005 and March 2006 at the Artificial Intelligence Laboratory of FEI in São Bernardo do Campo, São Paulo, Brazil. It consists of 400 images of 200 Brazilian individuals (100 males and 100 females), aged 19 to 40, displaying neutral and smiling expressions, and the images have a 640×480 pixels resolution. Third, the London Face Research Laboratory (FRL) dataset includes 102 adult face images from 49 females and 53 males, aged 18 to 54, representing various racial backgrounds such as White, Black, and Asian. Each subject was photographed with natural and smiling expressions, and the image resolution is 1350×1350 pixels.

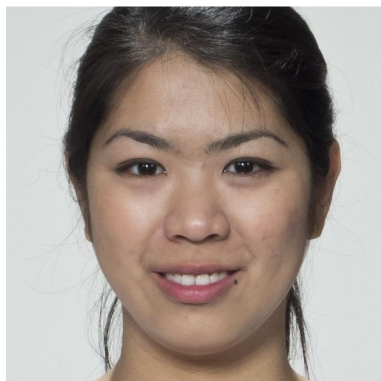


Supplementary Figure 31. The process of generating REAL depth images, including the software packages and data processing. The original face images are cropped into square formats to avoid distortion of the face landmark point cloud when using MediaPipe Face Landmarker. Without this preprocessing step, the landmark points may become misaligned, resulting in inconsistencies between the facial shape and the point cloud. To ensure the completeness and accuracy of the facial point cloud, OpenCV's Cascade Classifier is utilized to detect faces and crop $1,000 \times 1,000$ pixel headshots. The detected face is highlighted with a red box, and a green dot marks the center of the crop. Additionally, a blue circle surrounds the red box to define the cropping area, ensuring that the entire face is captured. The cropped image is processed using MediaPipe's Face Landmarker to detect facial landmarks. The resulting point cloud of facial landmarks is then utilized for further processing into depth images. First, to compensate for head tilt, the line between the eye centers is aligned horizontally by computing its slope and using the arctangent to determine the rotation angle. All points are then rotated using the rotation matrix. Second, the scale of the RANDOM is well-defined in simulation software, whereas the REAL scale depends on the image resolution. To address this, we use the iris as a reference scale to upscale the REAL to match real-world coordinate systems. The subsequent process for generating depth images is consistent with that of RANDOM.

Supplementary Table 3. Face landmark point numbers in MediaPipe

Face feature	Point numbers
Center of eyes	Left: [473], right: [468]
Iris	Left: [474, 476], right: [469, 471]
Eye_X = Eye_Y	[362, 398, 384, 385, 386, 387, 388, 466, 263, 249, 390, 373, 374, 380, 381, 382]
Nostril_X	[4, 4, 294, 294]
Nostril_Y	$[(4+1)/2, 2, 327, 294]$ *Add the values of No. 4 and No. 1, then divide by 2
Mouth_X	[4, 4, 317, 402, 318, 324, 308, 415, 310, 311, 312]
Mouth_Y	[13, 14, 317, 402, 318, 324, 308, 415, 310, 311, 312]

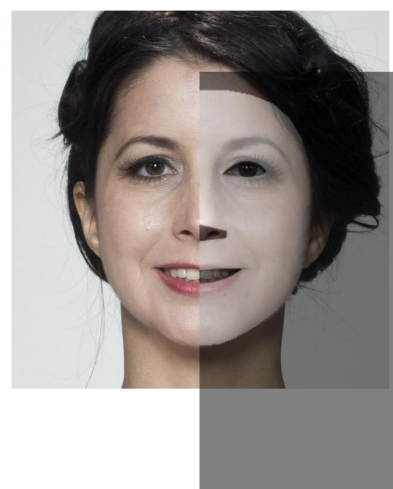
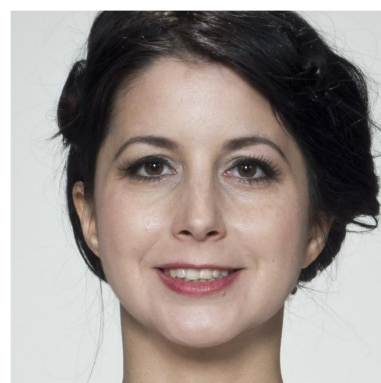
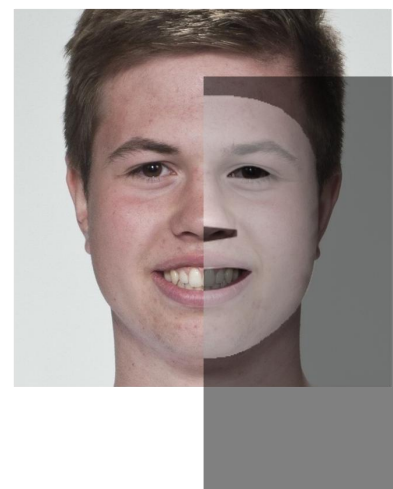
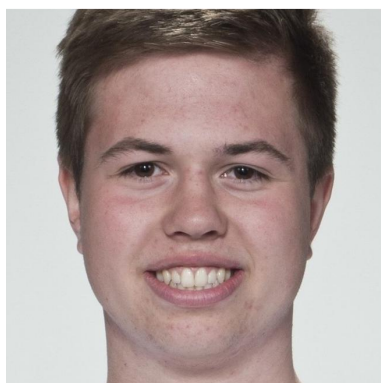
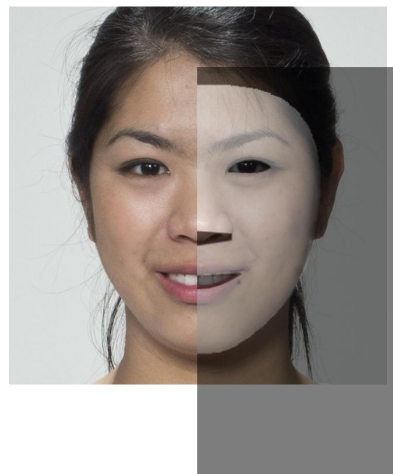
Crop Image



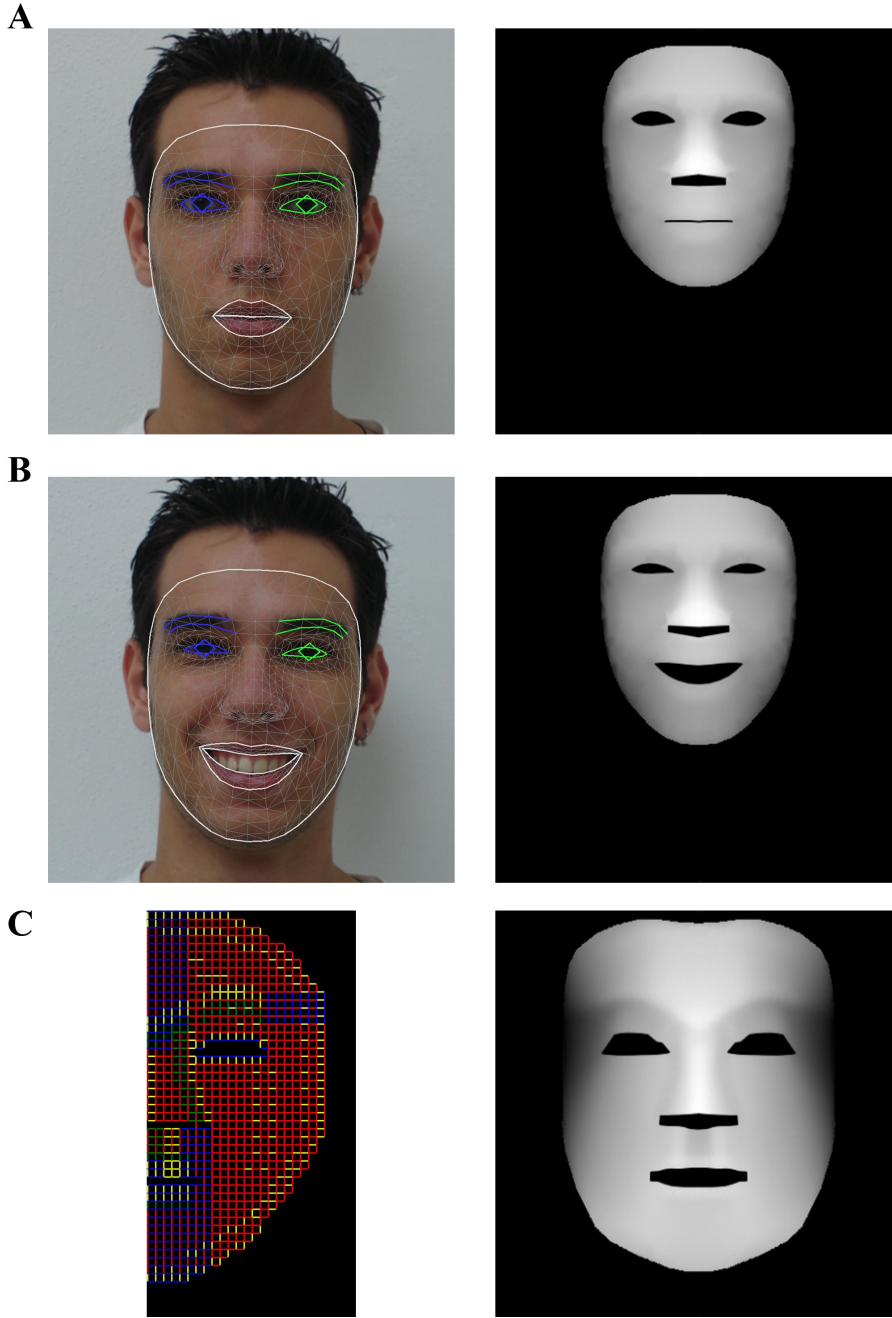
Depth Image



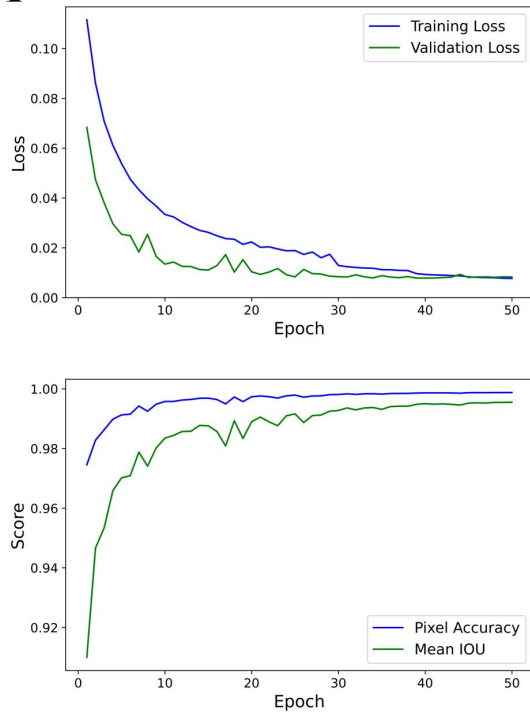
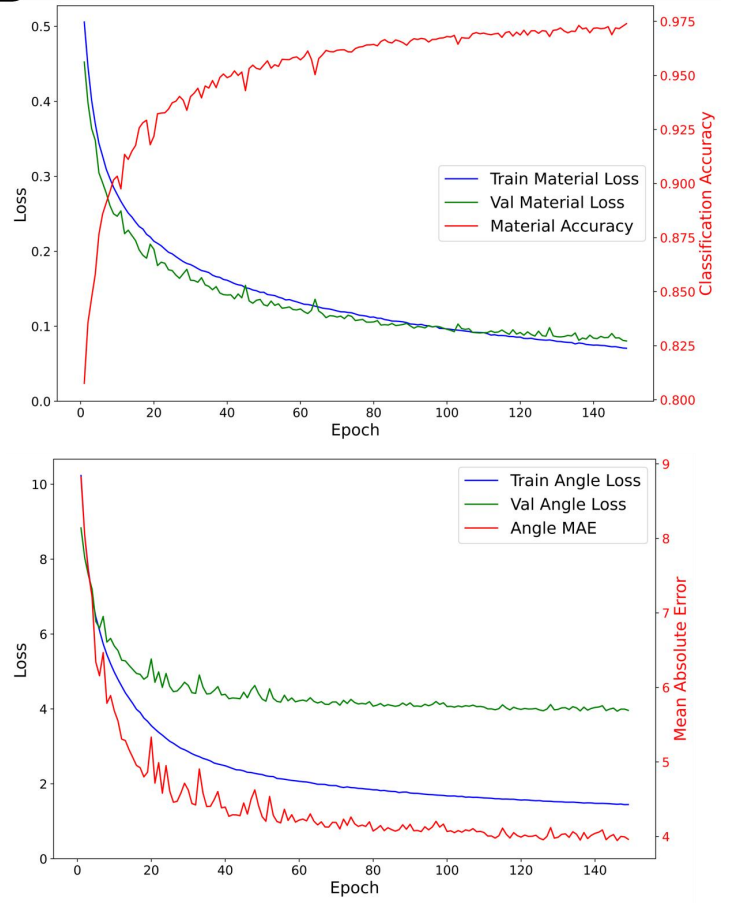
Overlay



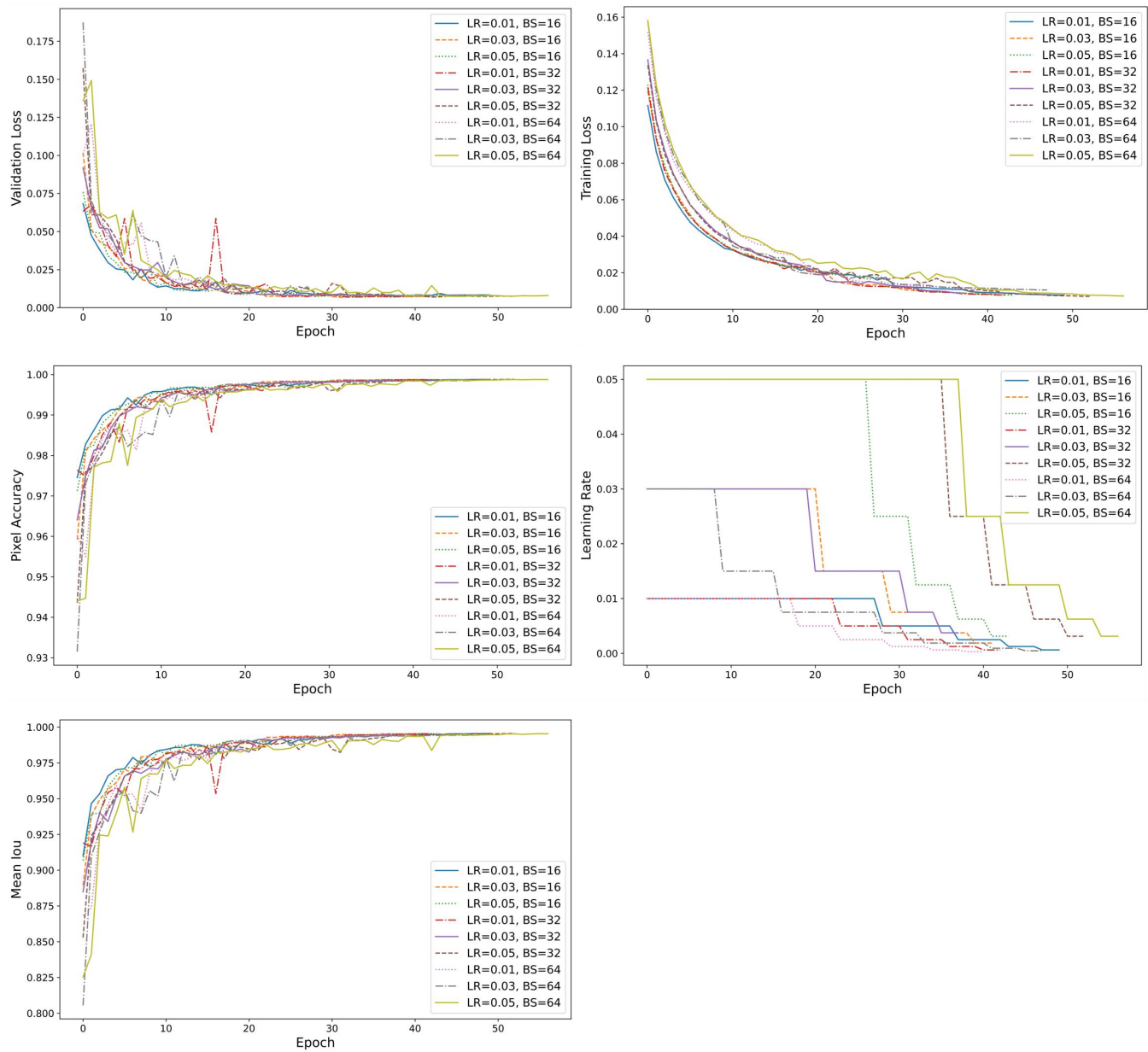
Supplementary Figure 32. Overlays of the RGB face images and their corresponding depth image to validate the accuracy and enhance data credibility.



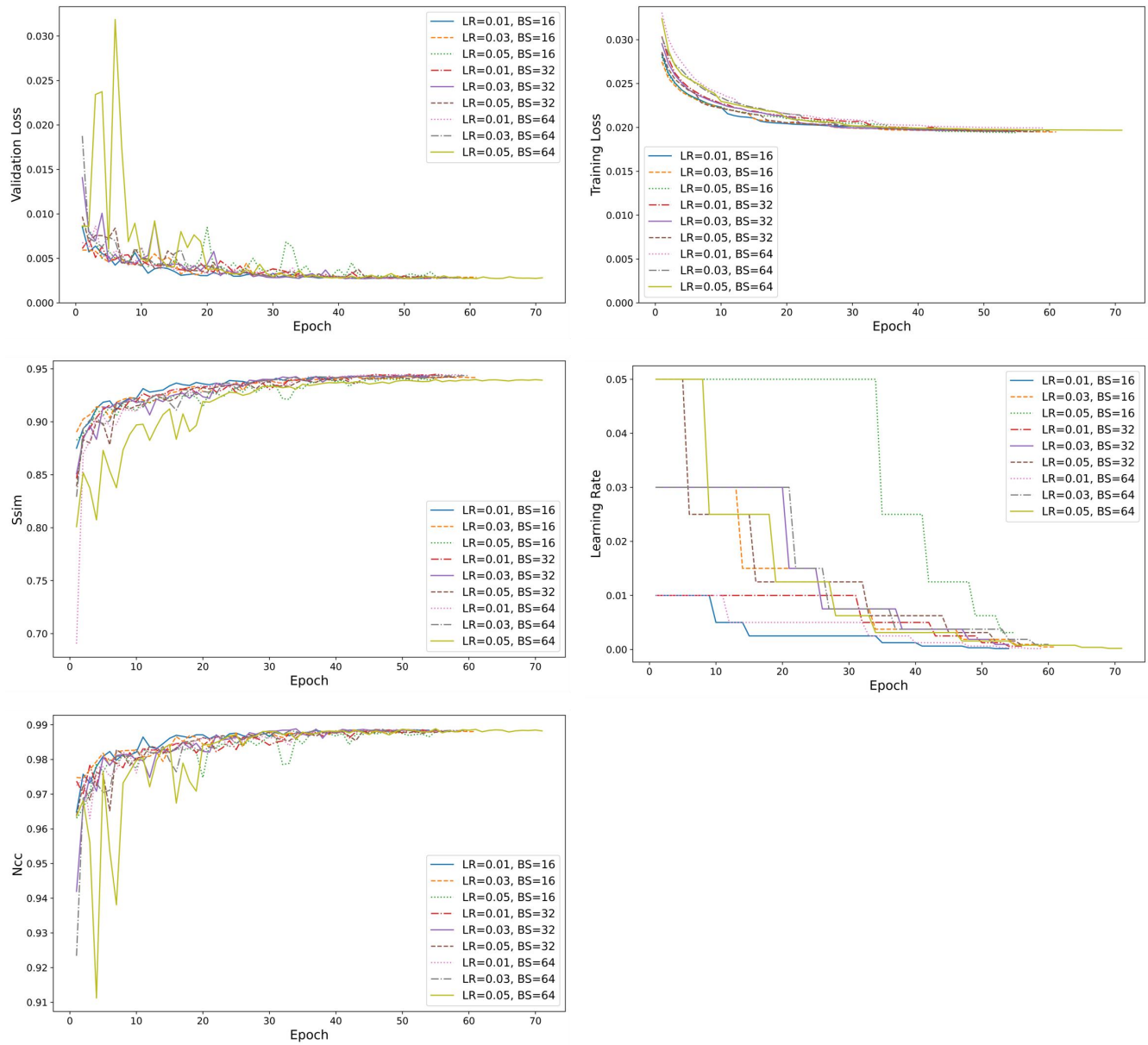
Supplementary Figure 33. (A) Neutral expression, (B) smiling expression. (C) Mouth height of the RANDOM mask equals one grid unit. The 1,270 facial images used in this study exhibit high diversity, covering a wide age range from 17 to 65 years, ensuring representation across different age groups. Furthermore, the dataset includes individuals from multiple ethnic backgrounds, enhancing racial diversity and allowing the model to generalize across different populations. The image resolutions vary from 640×480 to $2,444 \times 1,718$ pixels, enabling analysis under different image quality conditions, thereby improving the robustness of the experimental methodology. The dataset includes neutral and smiling expressions, representing fundamental facial expressions as an initial direction for experimentation.

A**B**

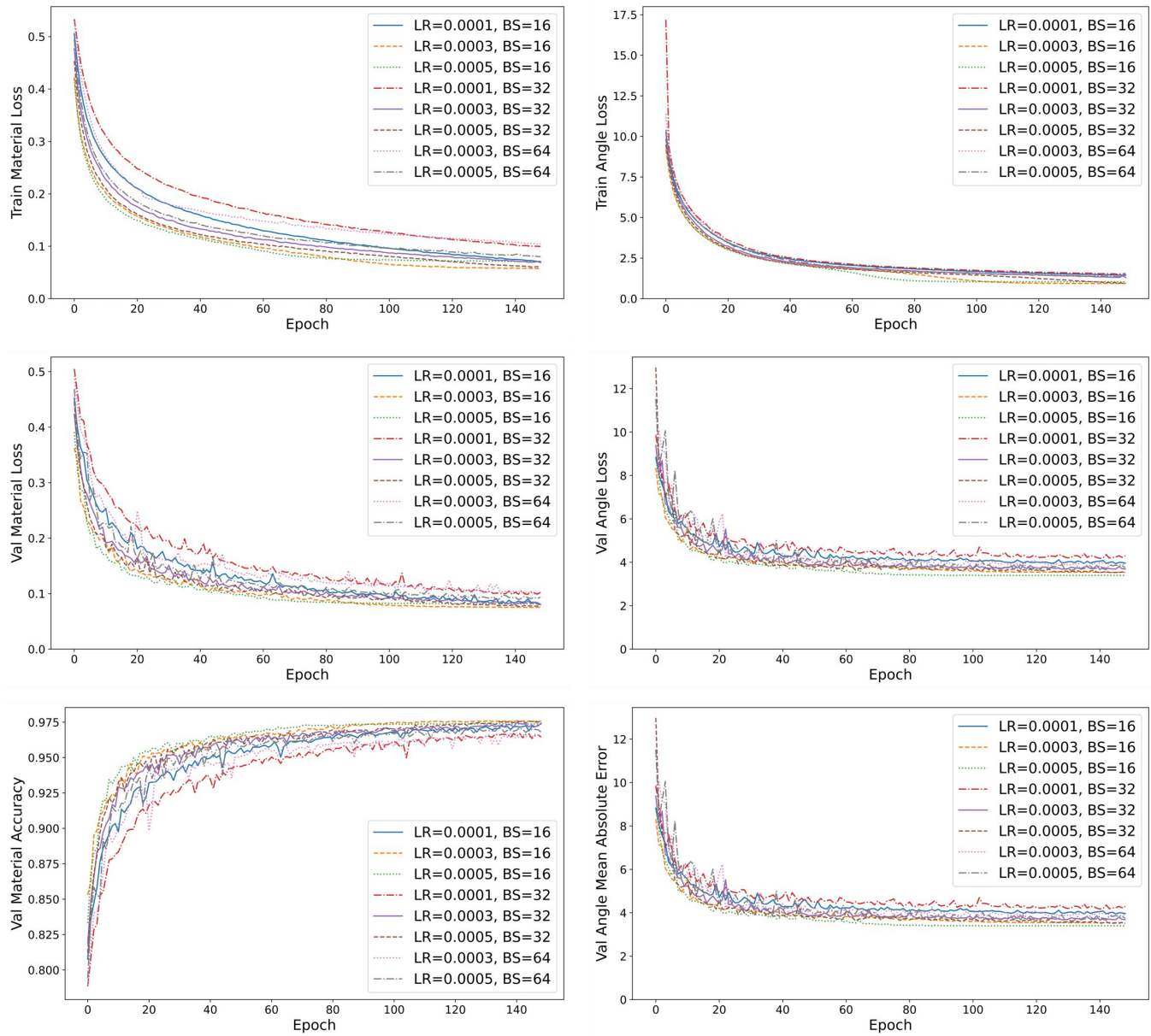
Supplementary Figure 34. Trends of the metrics in this study consistent with the validation loss: (A) pixel accuracy and mean IOU; (B) classification accuracy and mean absolute error.



Supplementary Figure 35. Learning curve, pixel accuracy, mean IOU, and scheduled learning rate of multiple hyperparameter combination models for the line matrix inverse design.

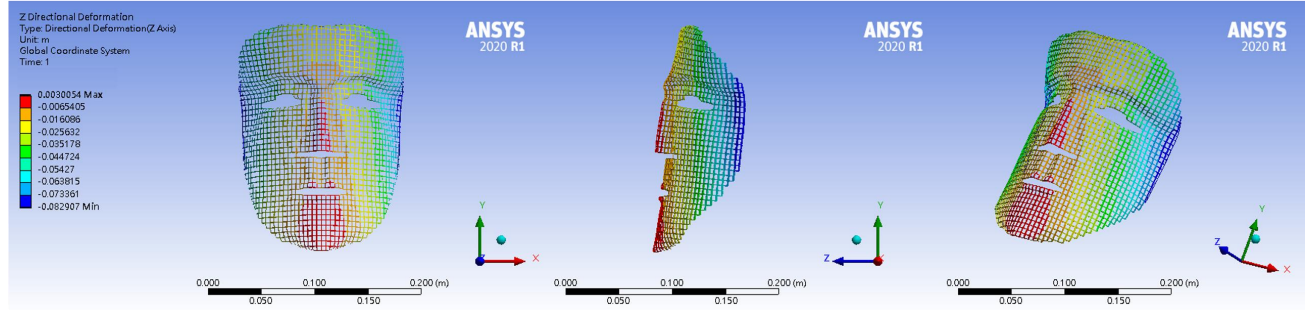


Supplementary Figure 36. Learning curve, SSIM, NCC, and scheduled learning rate of multiple hyperparameter combination models for forward prediction.

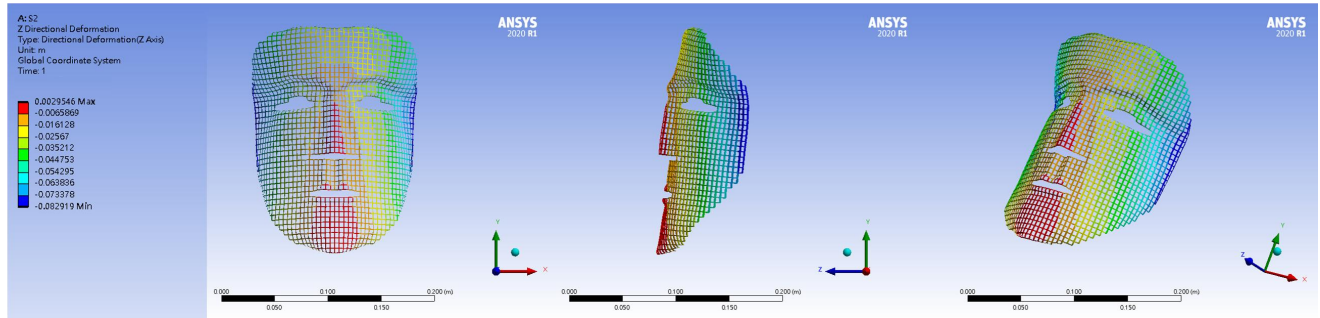


Supplementary Figure 37. Learning curve, classification accuracy, and mean absolute error of multiple hyperparameter combination models for the curve matrix inverse design.

A

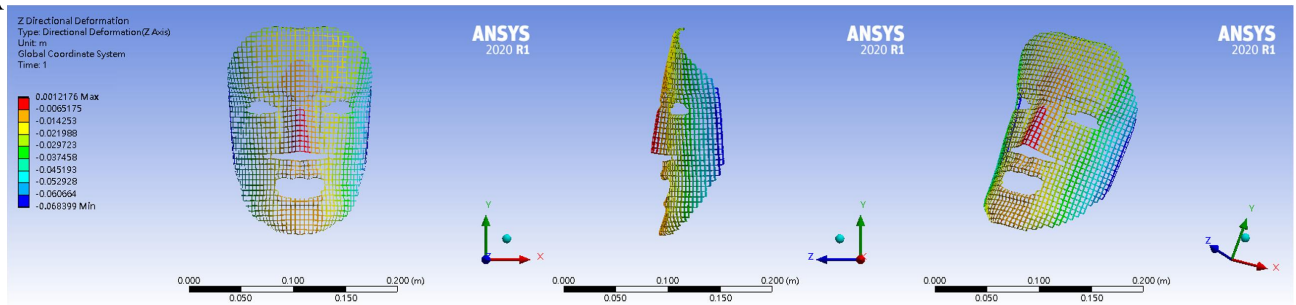


B

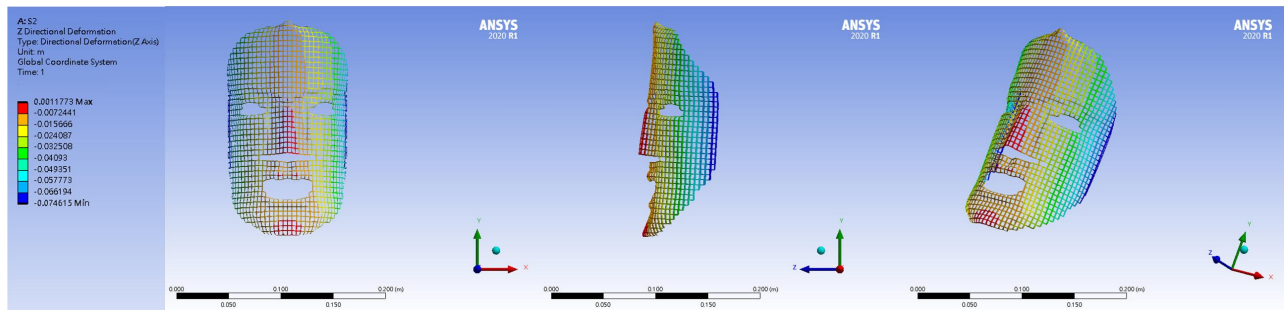


Supplementary Figure 38. First sample of line matrix inverse design: (A) Simulation. (B) Inferred simulation.

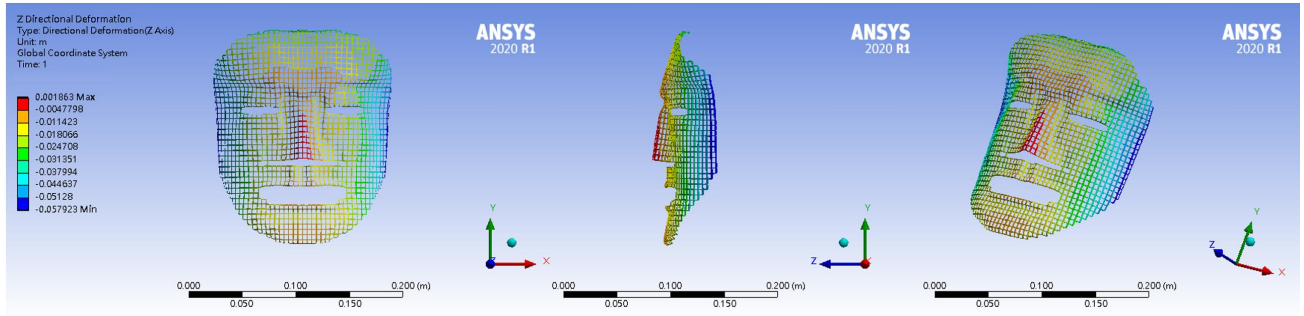
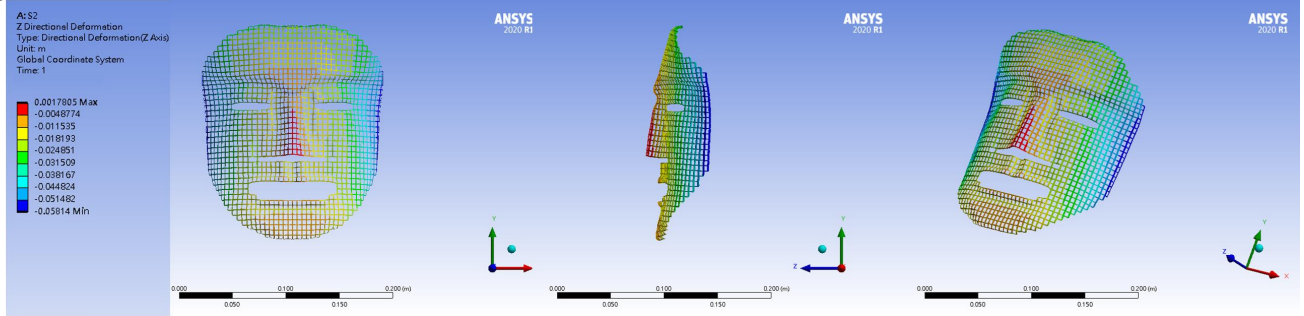
A



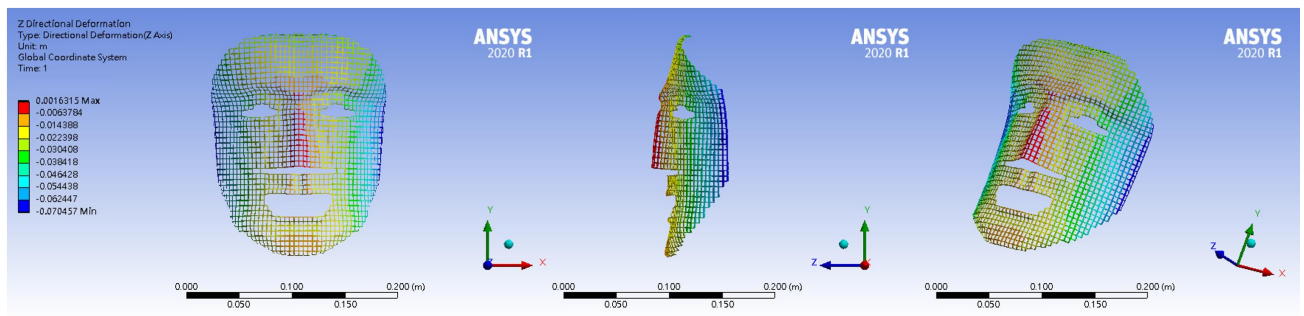
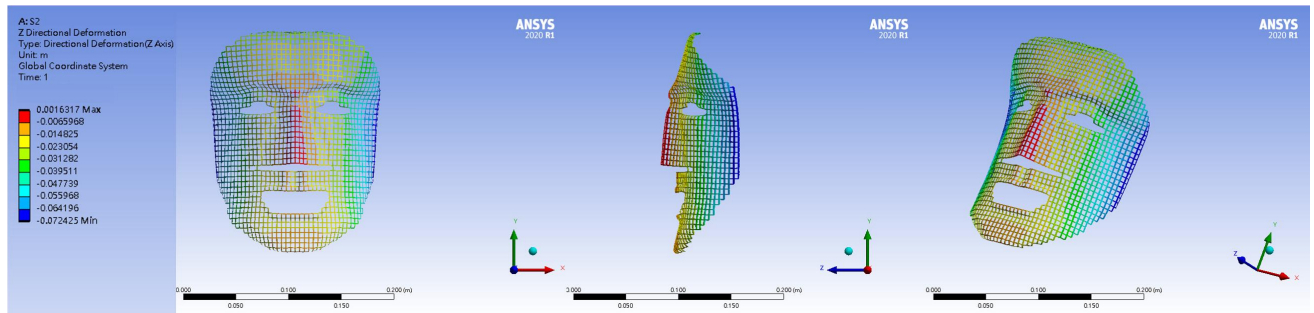
B



Supplementary Figure 39. Second sample of line matrix inverse design: (A) Simulation. (B) Inferred simulation.

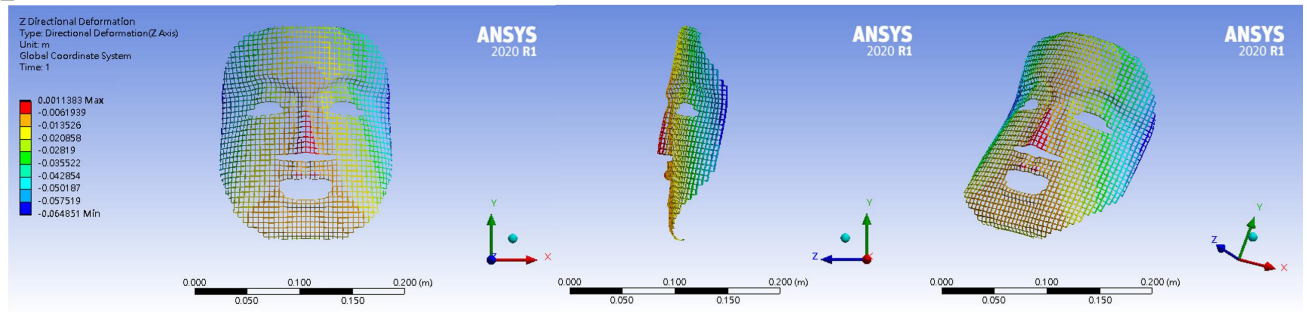
A**B**

Supplementary Figure 40. Third sample of line matrix inverse design: (A) Simulation. (B) Inferred simulation.

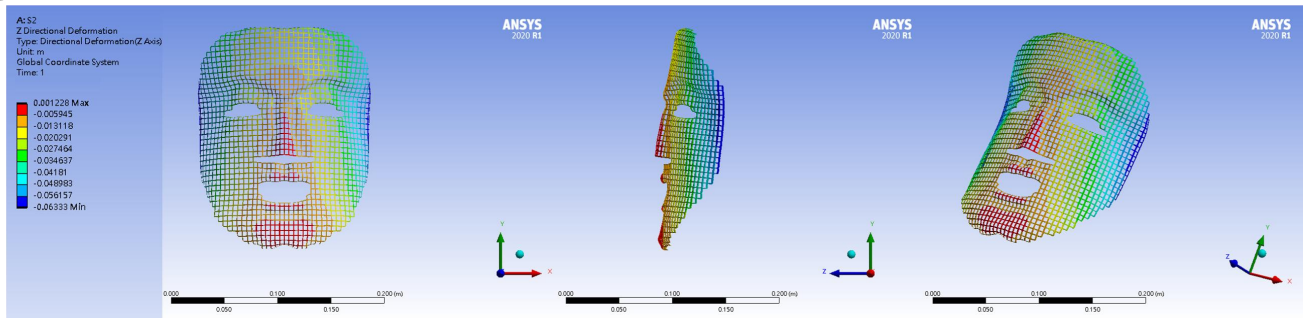
A**B**

Supplementary Figure 41. Fourth sample of line matrix inverse design: (A) Simulation. (B) Inferred simulation.

A



B



Supplementary Figure 42. Fifth sample of line matrix inverse design: (A) Simulation. (B) Inferred simulation.

Supplementary Table 4. RANDOM testing sets to evaluate the inverse design capabilities of the line matrix

		Mean	Median	1 STD	Max	Min
Grid Design	Mean IOU	0.9947	1	0.0137	1	0.6593
	Pixel Accuracy	0.9986	1	0.0049	1	0.8733
Depth Image	SSIM	0.9799	0.9862	0.0272	1	0.7611
	NCC	0.9906	0.9975	0.0335	1	0.6121

Supplementary Table 5. RANDOM testing sets to evaluate the forward prediction capabilities of the line matrix

		Mean	Median	1 STD	Max	Min
Depth Image	SSIM	0.9624	0.9727	0.0338	0.9878	0.7040
	NCC	0.9901	0.9976	0.0297	0.9970	0.6872

Supplementary Table 6. RANDOM testing sets to evaluate the inverse design capabilities of the curve matrix

		Mean	Median	1 STD	Max	Min
Rib Design	Accuracy	0.9732	1	0.0424	1	0.5455
	MAE	3.3270	2.9394	2.1921	32.3939	0.9091
Depth Image	SSIM	0.9839	0.9909	0.0275	0.9982	0.7899
	NCC	0.9861	0.9979	0.0545	0.9999	0.5474

Supplementary Table 7. Metrics results of the first three models using the RANDOM testing set

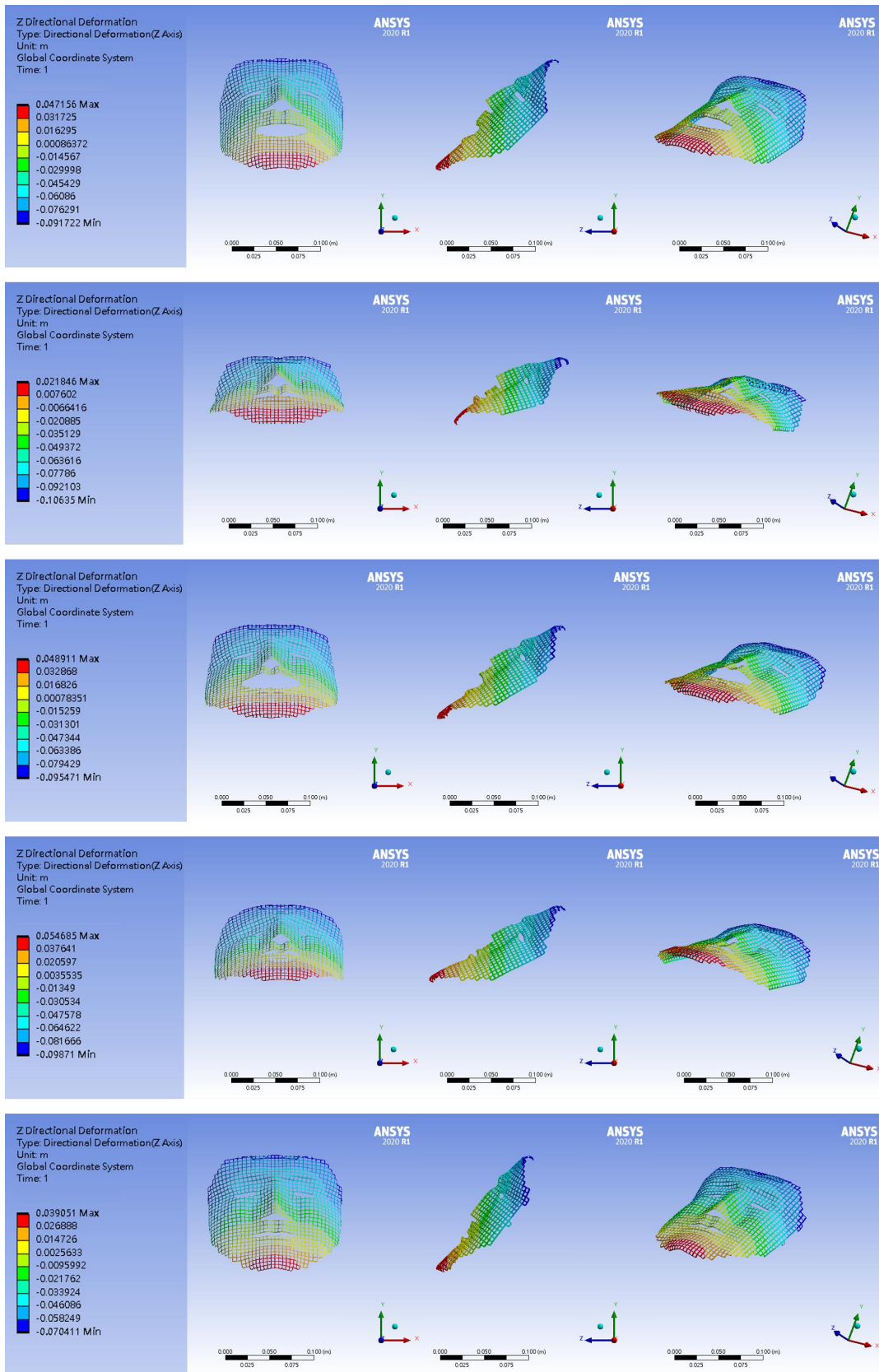
LR	BS	Number			Mean	Median	1 STD	Max	Min
0.01	16	2065	Grid Design	Mean IOU	0.996031	1	0.009917	1	0.869856
				Pixel Accuracy	0.998951	1	0.003447	1	0.943667
			Depth Image	SSIM	0.988707	0.998254	0.023848	1	0.798173
				NCC	0.994304	0.999902	0.026672	1	0.680879
0.01	32	2059	Grid Design	Mean IOU	0.994841	1	0.010475	1	0.893166
				Pixel Accuracy	0.998751	1	0.003389	1	0.946387
			Depth Image	SSIM	0.983735	0.995487	0.029961	1	0.774965
				NCC	0.990590	0.999617	0.036556	1	0.649378
0.01	64	2047	Grid Design	Mean IOU	0.994794	1	0.011798	1	0.883745
				Pixel Accuracy	0.992042	1	0.004289	1	0.959038
			Depth Image	SSIM	0.981206	0.997629	0.027945	1	0.769482
				NCC	0.994830	0.999753	0.032129	1	0.682034

Supplementary Table 8. Metrics results of the middle three models using the RANDOM testing set

LR	BS	Number			Mean	Median	1 STD	Max	Min
0.03	16	2068	Grid Design	Mean IOU	0.995246	1	0.011864	1	0.748922
				Pixel Accuracy	0.998779	1	0.004042	1	0.916861
			Depth Image	SSIM	0.986104	0.997223	0.027877	1	0.774015
				NCC	0.992244	0.999813	0.032014	1	0.688994
0.03	32	2043	Grid Design	Mean IOU	0.995420	1	0.010248	1	0.881649
				Pixel Accuracy	0.998788	1	0.003611	1	0.944833
			Depth Image	SSIM	0.986433	0.997529	0.027210	1	0.742316
				NCC	0.992654	0.999829	0.031640	1	0.593884
0.03	64	2048	Grid Design	Mean IOU	0.994099	1	0.010983	1	0.759378
				Pixel Accuracy	0.993811	1	0.003256	1	0.920382
			Depth Image	SSIM	0.988934	0.997123	0.029842	1	0.740215
				NCC	0.990381	0.999895	0.036688	1	0.693841

Supplementary Table 9. Metrics results of the last three models using the RANDOM testing set

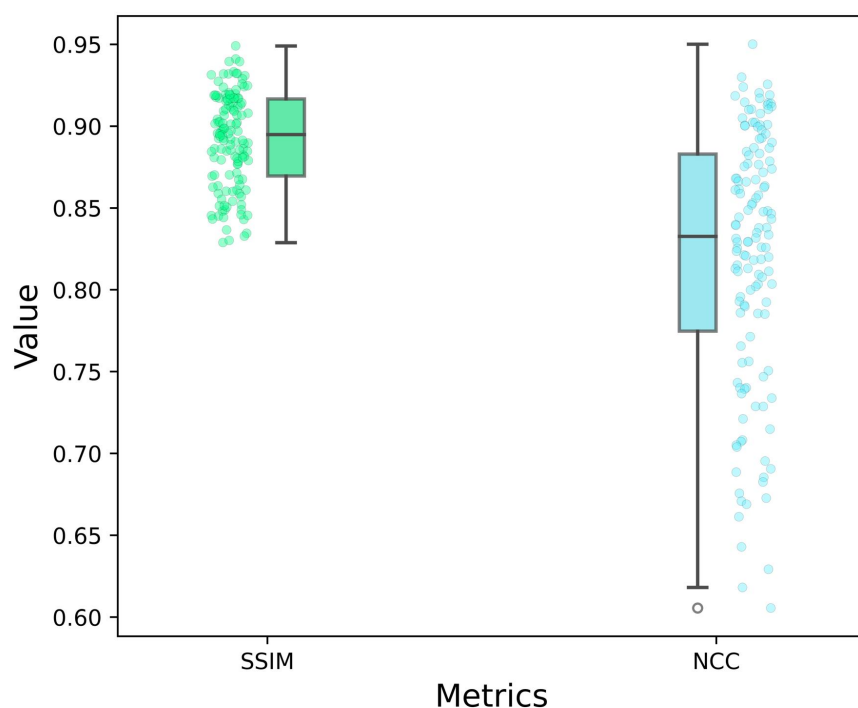
LR	BS	Number			Mean	Median	1 STD	Max	Min
0.05	16	1,992	Grid Design	Mean IOU	0.994925	1	0.012347	1	0.739345
				Pixel Accuracy	0.998681	1	0.004129	1	0.916861
			Depth Image	SSIM	0.984922	0.997710	0.029695	1	0.754598
				NCC	0.991073	0.999851	0.036345	1	0.615045
0.05	32	2,058	Grid Design	Mean IOU	0.995279	1	0.010854	1	0.865221
				Pixel Accuracy	0.998806	1	0.003743	1	0.939005
			Depth Image	SSIM	0.986257	0.997241	0.027006	1	0.705155
				NCC	0.992508	0.999807	0.031610	1	0.566864
0.05	64	2,050	Grid Design	Mean IOU	0.995658	1	0.010254	1	0.838375
				Pixel Accuracy	0.992394	1	0.003548	1	0.949378
			Depth Image	SSIM	0.984951	0.995846	0.027512	1	0.724948
				NCC	0.993086	0.999884	0.031595	1	0.593841



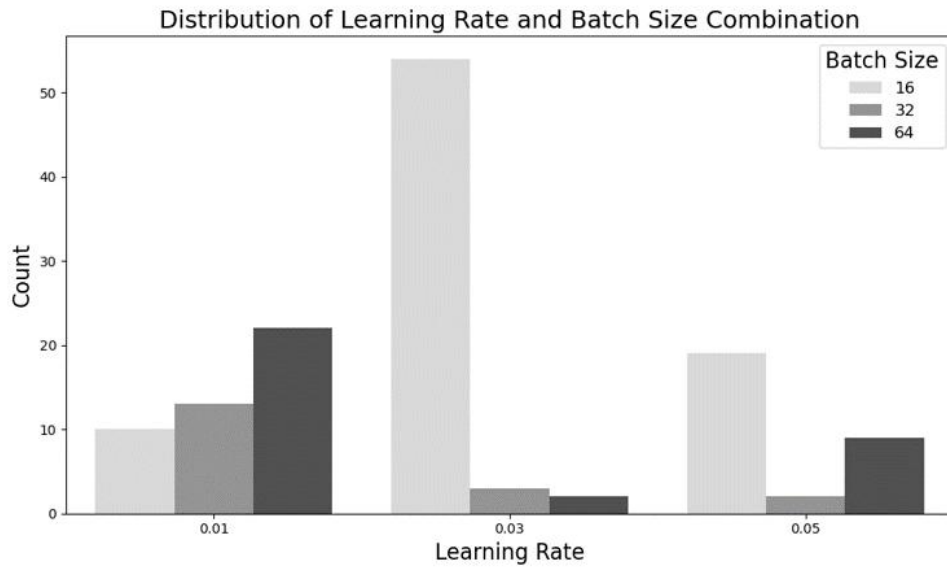
Supplementary Figure 43. Simulated results of the manually inferred grid designs for five facial cases.

Supplementary Table 10. Similarity metric between 134 target shapes and the inferred depth images

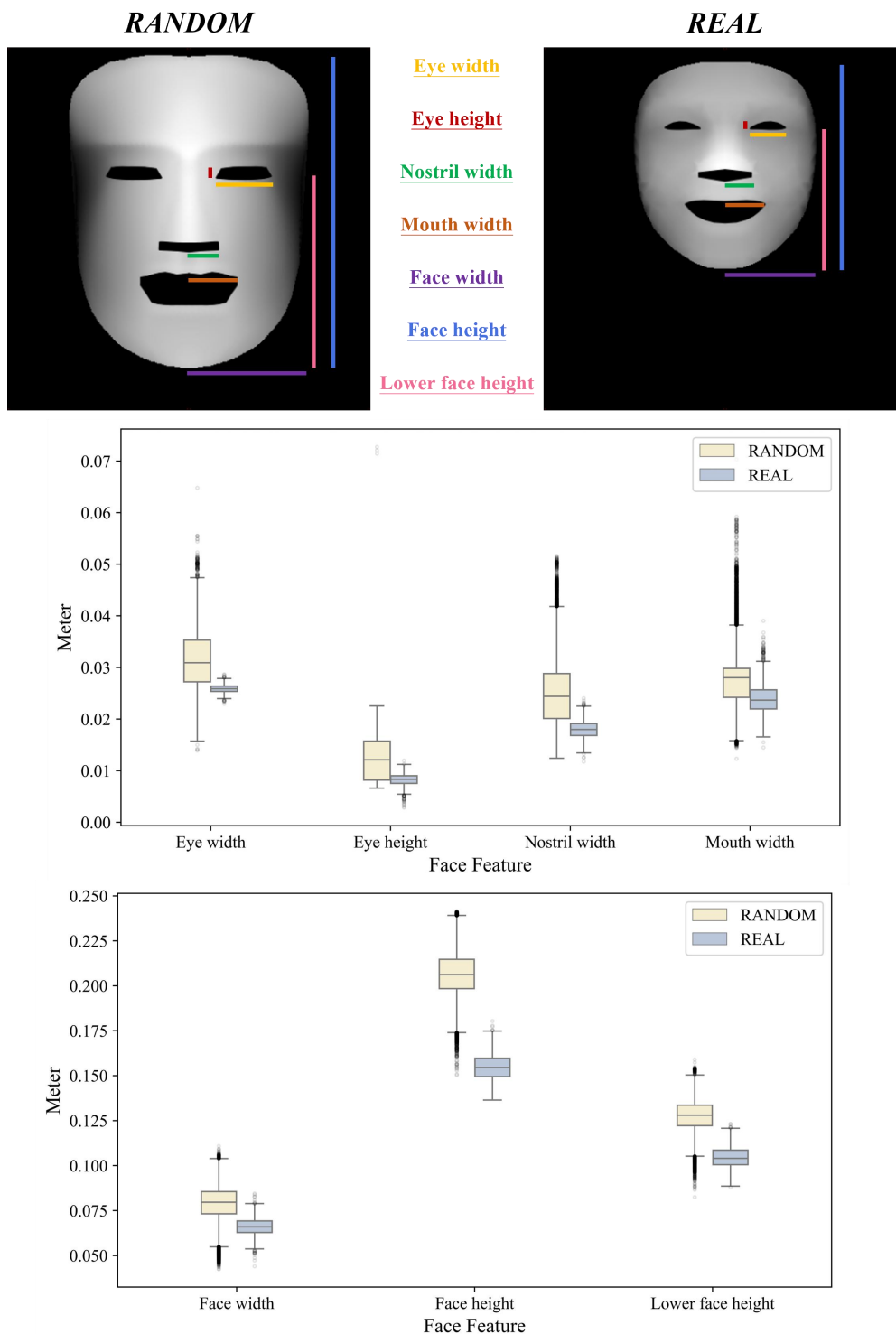
		Mean	Median	STD	Max	Min
Depth Image	SSIM	0.891346	0.894867	0.028798	0.949021	0.828835
	NCC	0.819892	0.832596	0.078811	0.950045	0.605503



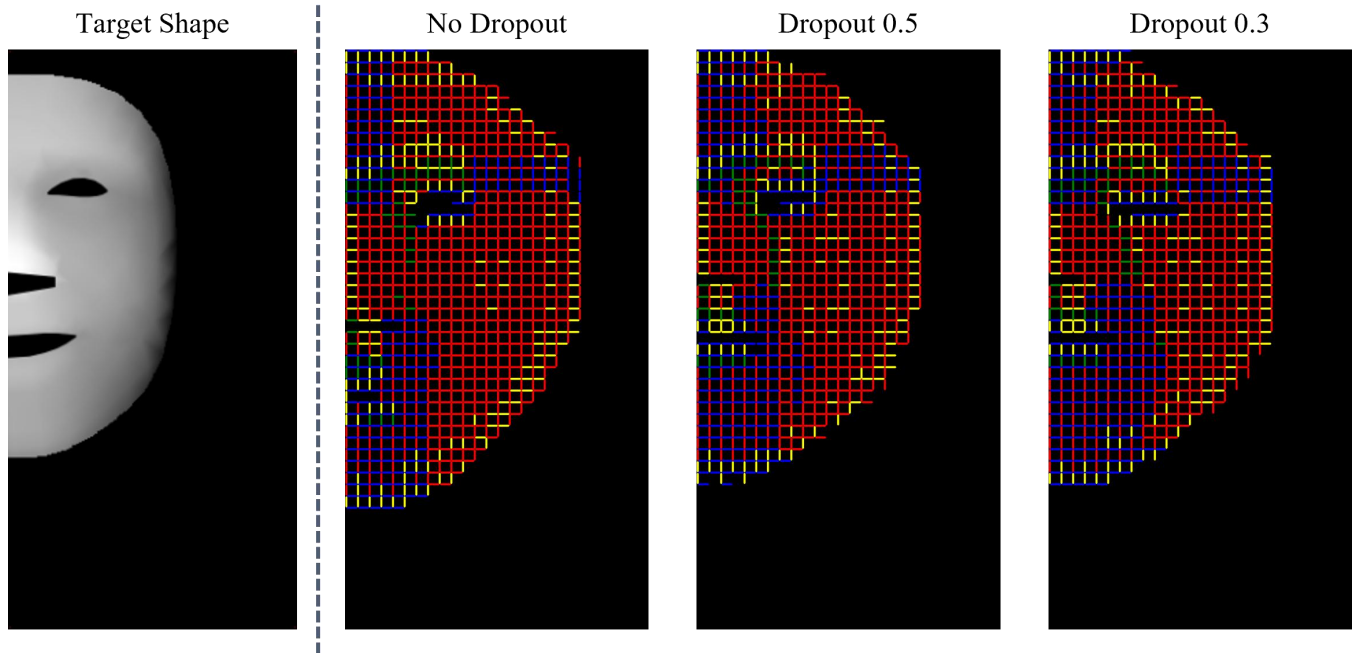
Supplementary Figure 44. Scatter plot and box plot of the similarity metric between 134 target shapes and the inferred depth images.



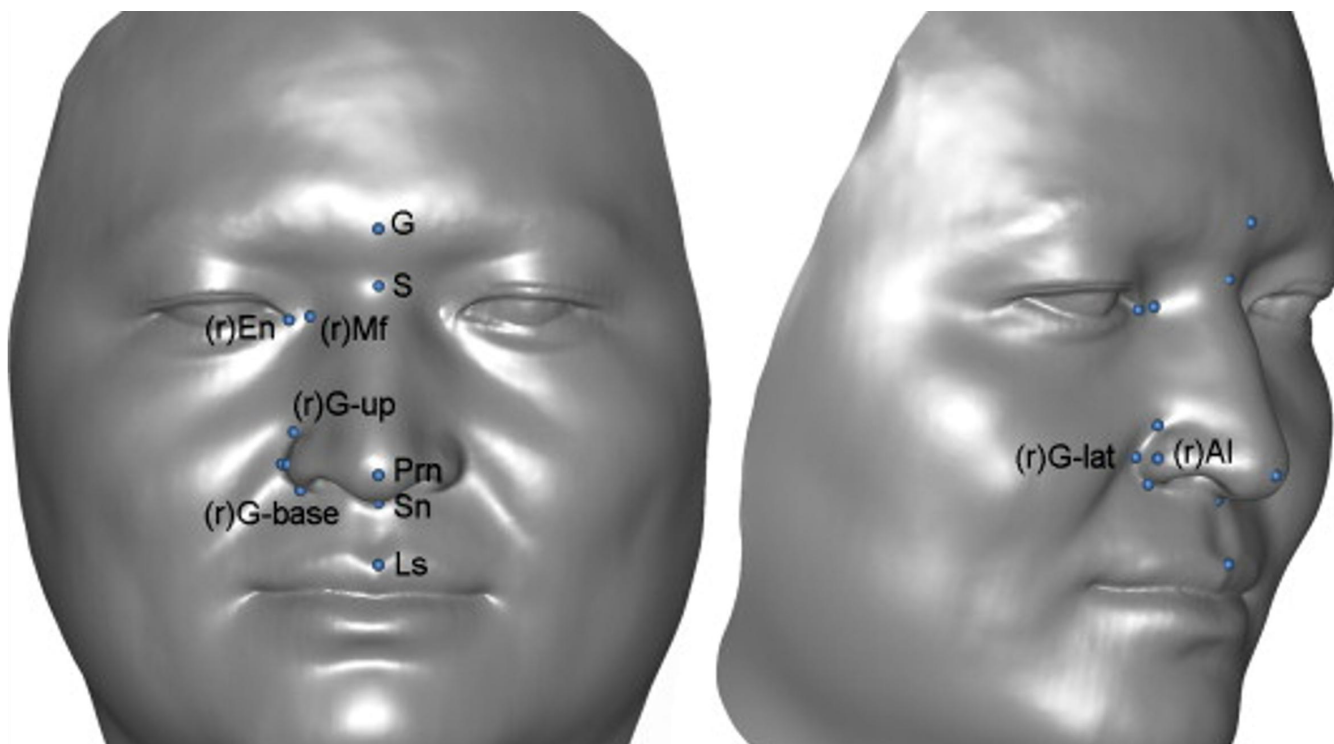
Supplementary Figure 45. The highest-scoring hyperparameter combination for each of the 134 faces.



Supplementary Figure 46. Comparison of facial feature scales between RANDOM and REAL. In the RANDOM dataset, conditional statements were designed for simulation nodes to identify the corresponding node numbers, enabling the calculation of these feature scales. In the REAL dataset, the 3D coordinates of facial landmark points were scaled using the iris as a reference, allowing for comparable measurements.

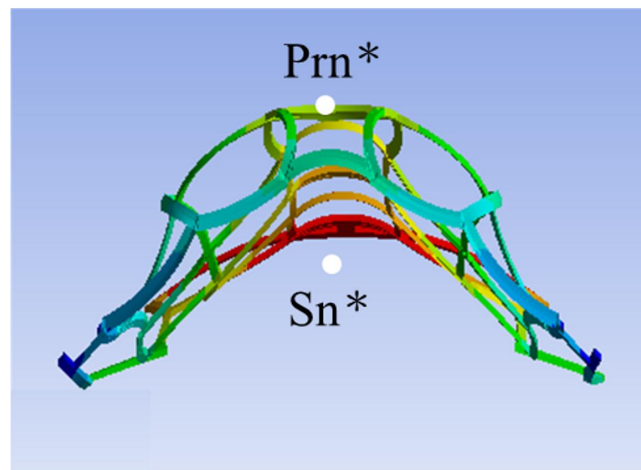
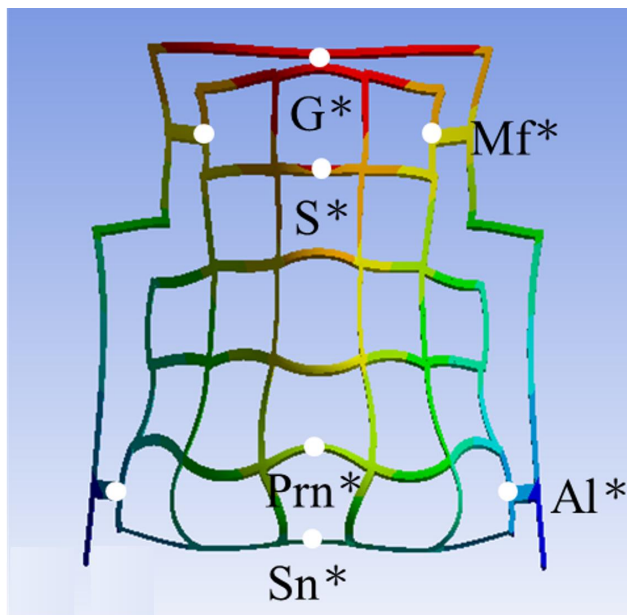


Supplementary Figure 47. Inferred grid design using different dropout settings for the same target shape.



Landmark	Symbol	Definition
Glabella	G	The most prominent midline point between the eyebrows on the forehead.
Sellion	S	The deepest point at the nasofrontal angle.
Maxillofrontale	Mf	The point where the frontomaxillary and nasal sutures meet.
Pronasale	Prn	The most protruding point on the tip of the nose.
Subnasale	Sn	The midpoint where the nasal septum and the upper lip meet.
Alar	Al	The most lateral point on the surface of the alar (nostril wing).

Supplementary Figure 48. ix primary nasal landmarks selected and mapped in this study: glabella (G), sellion (S), maxillofrontale (Mf), pronasale (Prn), subnasale (Sn), and alare (Al).

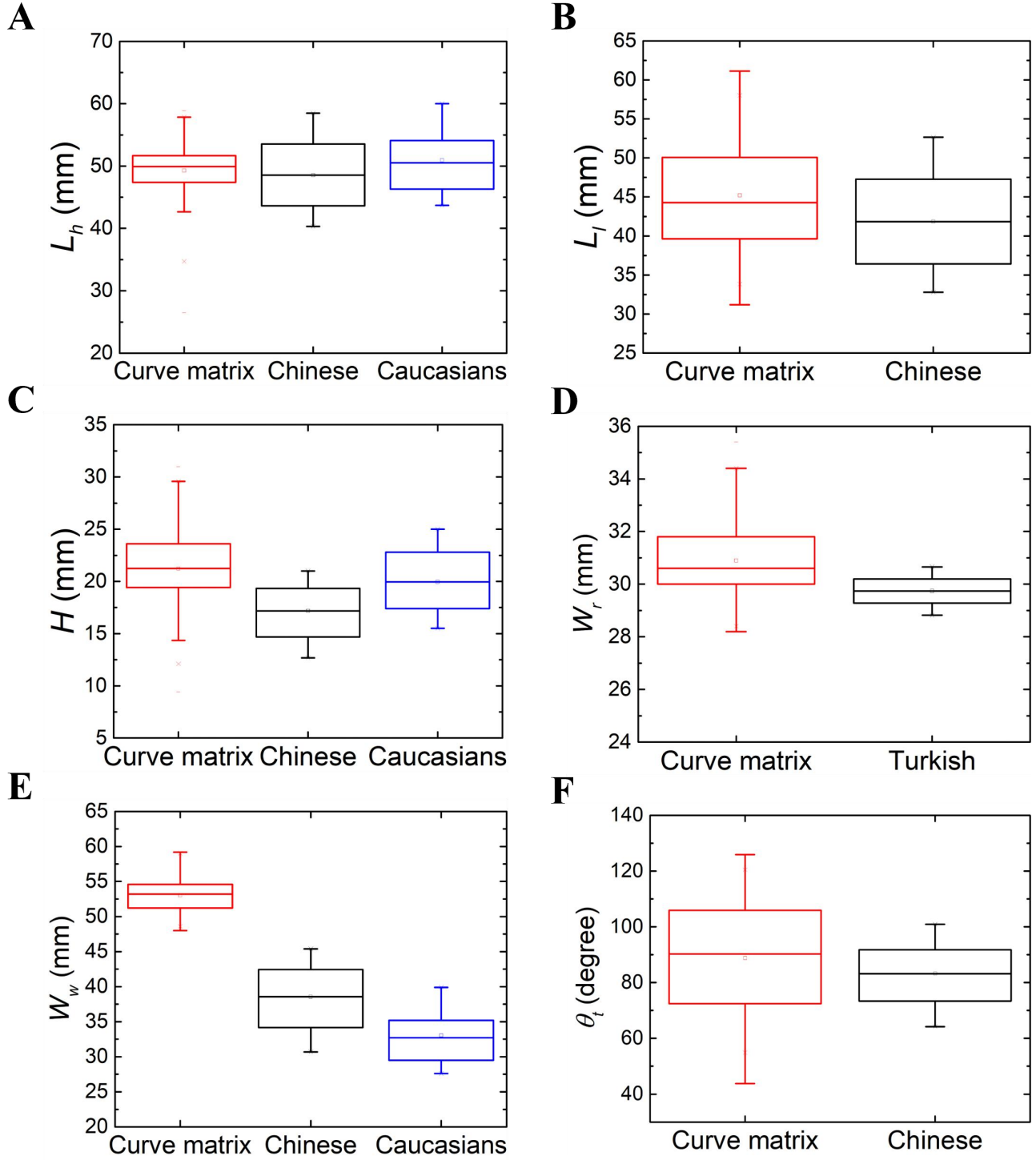


Landmark	Symbol	Definition
Glabella	G*	Connection point with the connecting frame.
Sellion	S*	Deepest point at the base of the nasal root angle.
Maxillofrontale	Mf*	Connection point with the connecting frame.
Pronasale	Prn*	Most protruding point on the nasal tip.
Subnasale	Sn*	Terminal projection onto the xy-plane of the nasal curve mesh coordinates.
Alar	Al*	Connection point with the connecting frame.

Supplementary Figure 49. Anatomical landmark positions accurately adjusted and redefined to ensure proper alignment, as the curve matrix encompasses only the nasal area.

Supplementary Table 11. Quantitative names and measurement methods

Quantitative name	Symbol	Measurement
Nasal height	L_h	Straight-line distance from S* to Sn*
Nasal length	L_l	Straight-line distance from S* to Prn*
Nasal tip protrusion	H	Straight-line distance from Prn* to Sn*
Nasal root width	W_r	Straight-line distance from Mf* to Mf*
Nasal width	W_w	Straight-line distance from Al* to Al*
Nasal tip angle	θ_t	The angle between Prn* and S* to Sn*



Supplementary Figure 50. Selected datasets for comparison based on balanced gender ratios, diverse ethnicities, large sample sizes, and comprehensive measurement items. (A) Nasal height^[2,3]. (B) Nasal length^[2]. (C) Nasal tip protrusion^[2,3]. (D) Nasal root width^[4]. (E) Nasal width^[2,3]. (F) Nasal tip angle^[2].

Supplementary Table 12. Statistical analysis of Z-axis deviation at each point in the line matrix

Points number	Mean	Median	1 STD	Max	Min
531	6.5166	6.0531	4.9163	29.2989	0.0651
450	3.5239	2.6108	3.1523	16.2044	0.0038
501	6.2675	4.6259	5.4833	26.9606	0.0066

Supplementary Table 13. Statistical analysis of Z-axis deviation at each point in the curve matrix

Points number	Mean	Median	1 STD	Max	Min
80	2.6225	2.0225	1.8789	7.1499	0.0412
78	2.6008	2.3812	1.5711	5.9288	0.0196
75	1.7181	1.5381	1.2430	5.7516	0.0863

References

1. Boley, J.W.; Van Rees, W.M.; Lissandrello, C.; Horenstein, M.N.; Truby, R.L.; Kotikian, A.; Lewis, J.A.; Mahadevan, L. Shape-shifting structured lattices via multimaterial 4D printing. *Proceedings of the National Academy of Sciences* **2019**, *116*, 20856-20862.
2. Aung, S.C.; Liam, F.C.; Teik, L.S. Three dimensional laser scan assessment of the Oriental nose with a new classification of Oriental nasal types. *British journal of plastic surgery* **2000**, *53*, 109-116.
3. Farkas, L.G. Anthropometry of the head and face. *(No Title)* **1981**.
4. Uzun, A.; Akbas, H.; Bilgic, S.; Emirzeoglu, M.; Bostancı, O.; Sahin, B.; Bek, Y. The average values of the nasal anthropometric measurements in 108 young Turkish males. *Auris Nasus Larynx* **2006**, *33*, 31-35.